7

Electromagnetic Calorimeter

7.1 Physics Requirements and Performance Goals

The introduction of high resolution, highly efficient CsI calorimeters has already led to major advances in the areas of conventional B meson, charmed meson, charmed baryon, and τ physics at the $\Upsilon(4S)$ [Sch94]. CsI calorimetry is also ideally suited to the primary physics goals of the BaBar detector, which require the tagging and reconstruction of B events containing CP eigenstate decays. The need to reconstruct CP eigenstates containing one or more π^0 decays makes excellent electromagnetic calorimetry essential to the success of the experiment. High efficiency for low-energy photons is required to offset the small branching fractions typical of all CP eigenstates, and to make it possible to reconstruct final states containing several π^0s. Good energy and angular resolution improve the π^0 and B mass resolutions, in turn improving the signal-to-background ratios of these rare decays. By facilitating lepton identification (e/π and e/μ separation), the calorimeter also provides one of the tags needed for every CP analysis.

7.1.1 Physics Processes Influencing Performance Goals

Energy and Angular Resolution

The understanding of CP violation in the B meson system requires the reconstruction of final states such as $B^0 \to J/\psi K_S^0$, $B^0 \to J/\psi K^{*0}$, $B^0 \to \rho^\pm\pi^\mp$, $B^0 \to D^+D^-$, $B^0 \to D^{*+}D^{*-}$, $B^0 \to \phi\pi^0$, and $B^0 \to K_S^0 K_S^0$. These channels either contain a direct π^0 or can be reconstructed through a decay chain containing one or more daughter π^0s. For example, the decay $K^{*0} \to K_S^0\pi^0$ occurs about one-sixth of the time (which is one-half of its decays to CP eigenstates), and many $D^\pm$ and $D^{*\pm}$ decays with large branching fractions contain π^0s.

Generic B decays contain an average of 5.5 charged tracks and 5.5 photons, with about 50% of the photon energies below 200 MeV (Figure 7-1(a)). Because the B meson is moving relatively slowly in the lab frame, the photon energy resolution, rather than the angular resolution, determines the B^0 mass resolution [Ale94b]. This is true even for the kinematically most

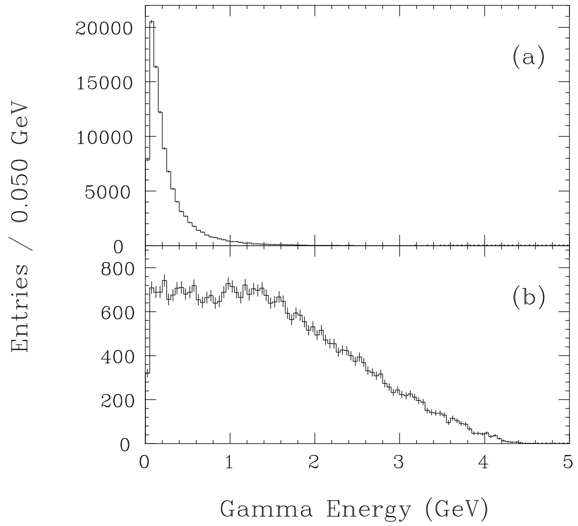

Figure 7-1. *Photon energy spectrum in (a) generic B decays and (b) $B^0 \to \pi^0\pi^0$ events.*

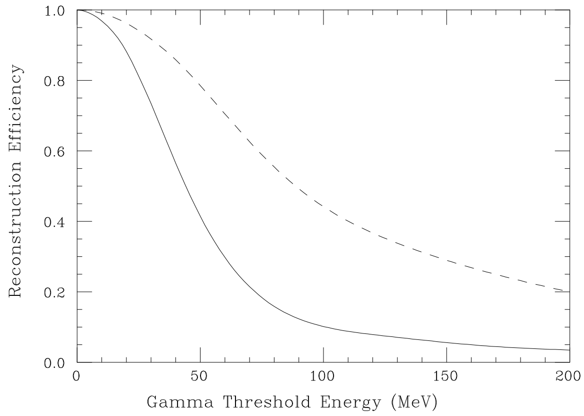

Figure 7-2. *π^0 (dashed line) and B meson reconstruction efficiency (solid line) vs. photon energy threshold for generic B decays. (Taken from reference [HEL92]. Efficiencies exclude geometric acceptance.)*

extreme channel of interest, $B^0 \to \pi^0\pi^0$ (used to untangle penguin contributions to $B^0 \to \pi^+\pi^-$), in which both π^0s have momenta above $1\,\mathrm{GeV}/c$, and photon energies extend up to 4.5 GeV (Figure 7-1(b)).

Photon Efficiency and Solid Angle Coverage

Sensitivity to low-energy photons is critical for efficient π^0 detection. The π^0 and B meson reconstruction efficiency for generic B decays, as a function of the minimum detectable photon energy, is shown in Figure 7-2. Reconstruction efficiency is also sensitive to solid angle coverage. The reconstruction efficiency, as a function of both the minimum and maximum measured photon energy and the minimum and maximum detectable polar angle, is shown in Figure 7-3 for (1) $B^0 \to \pi^0\pi^0$, producing four relatively high-energy photons, (2) $B^0 \to J/\psi K^0_S$, $K^0_S \to \pi^0\pi^0$, producing four relatively soft photons, and (3) $B^0 \to \rho^\pm\pi^\mp$, producing only two photons. Losses in the forward direction (Figure 7-3(a)) are not as severe as for low-multiplicity all-charged modes, though $\pi^0\pi^0$ is somewhat worse than $\pi^+\pi^-$. In the backward direction (Figure 7-3(b)) the demands on solid angle coverage are more modest.

Lepton tagging requires the calorimeter to reject pions misidentified as electrons to a level of $\sim 10^{-3}$.

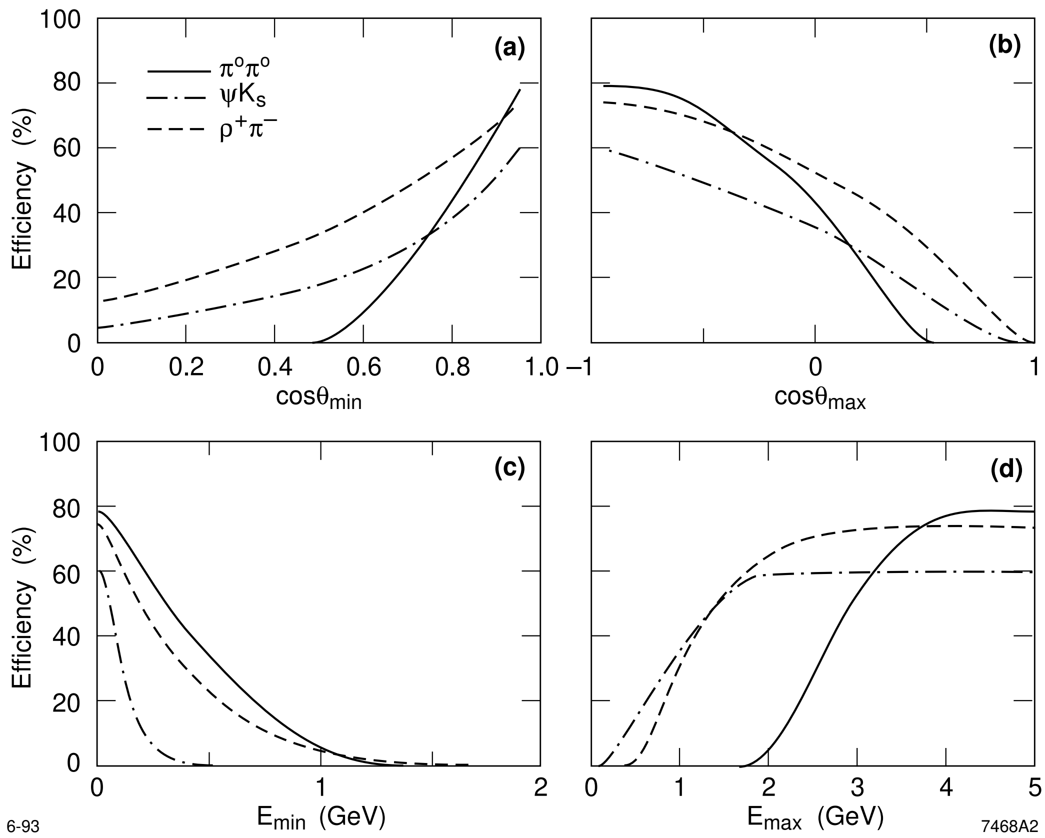

Figure 7-3. *Dependence of B reconstruction efficiency on (a) minimum detectable θ; (b) maximum detectable θ; (c) minimum detectable energy; and (d) maximum detectable energy for decay photons from $B^0 \to \pi^+\pi^-$ (solid), $B^0 \to J/\psi K^0_S$, $J/\psi \to \ell^+\ell^-$, $K^0_S \to \pi^0\pi^0$ (dash-dot), and $B^0 \to \rho^\pm\pi^\mp$, $\rho^\pm \to \pi^\pm\pi^0$ (dash).*

The requirements placed on the calorimeter by non-*CP* physics are generally similar to those from *CP* physics. One exception is the need for efficient tagging of outgoing leptons in two-photon events. A backward endcap, which would contribute little to overall B reconstruction efficiency, would be important for this purpose. Another exception occurs in low-multiplicity final states that do not arise from B decays (*e.g.,* Bhabha scattering, and charm and tau decays), for which the energy range can extend up to the higher beam energy. For these processes, leakage, and hence detector depth, is the primary consideration.

7.1.2 Summary of Performance Targets

These physics requirements lead to a calorimeter design based on quasi projective CsI(Tl) crystals over the entire available solid angle.

The target energy resolution for photons at a polar angle of 90° is:

$$\frac{\sigma_E}{E} = \frac{1\%}{\sqrt[4]{\mathrm{E(GeV)}}} \oplus 1.2\%. \tag{7.1}$$

The constant term arises from front and rear leakage ($\leq$ 1.0%), inter-calibration errors (0.25%) and light collection nonuniformity ($\leq$ 0.5%). This expression does not include electronic noise, which is estimated to be $\leq$ 150 keV per crystal in the proposed readout system, because this contribution is negligible for typical clusters of 16–25 crystals, even at low energies. The resolution degrades at small polar angles, as discussed in subsequent sections, as a consequence of the staggered arrangement of crystals.

For comparison, this performance represents a considerable improvement over that of the CLEO-II calorimeter. A number of factors contribute to the improvement: the use of projective geometry in the forward endcap, a reduction of back leakage and losses in inactive material in front of and between the crystals, and reduction of electronic noise (allowing more crystals to be summed). In addition, the usable solid-angle coverage has been increased.

The angular resolution is determined by the transverse crystal size and average distance to the interaction point. The target angular resolution is:

$$\sigma_\theta = \frac{3\,\mathrm{mr}}{\sqrt[2]{\mathrm{E(GeV)}}} \oplus 2\,\mathrm{mr}. \tag{7.2}$$

As in CLEO-II, the minimum detectable energy for photons is about 10–20 MeV. It is expected to be largely determined by beam- and event-related backgrounds in the calorimeter, since the intrinsic CsI(Tl) efficiency should be close to 100%, even at energies as low as a few MeV.

The solid angle coverage of the calorimeter extends from a polar angle of 250 mr in the forward direction ($\cos\theta = 0.97$) to $\pi - 653$ mr in the backward direction ($\cos\theta = -0.80$). A backward endcap has been designed to cover the angular range down to $\pi - 560$ mr, primarily for two-photon tagging. It is not included in the baseline detector, but is a candidate for a future upgrade.

The performance of the calorimeter is summarized in Table 7-1.

Parameter	*BaBar* Design Performance
$\frac{\sigma_E}{E}$ (Stochastic Term) at 90°	1%
$\frac{\sigma_E}{E}$ (Constant Term) at 90°	1.2%
σ_θ at 1 GeV at 90°	5 mr
Efficiency at 20 MeV at 90°	85%
Efficiency at 100 MeV at 90°	95%
π/e Rejection at 500 MeV/c	few$\times 10^{-3}$
Minimum Detectable Energy	10–20 MeV
Electronic Noise/Crystal	$\leq$150 keV

Table 7-1. *Target performance for the CsI(Tl) calorimeter.*

7.2 Calorimeter Overview

7.2.1 Technology Choice

The considerations leading to the choice of CsI(Tl) for the *BaBar* calorimeter are discussed in References [Ale94a] and [Hea94]. The *BaBar* physics goals require an electromagnetic calorimeter with excellent photon energy resolution and efficiency at low energies ($\leq$ 100 MeV). The calorimeter sits inside the solenoid and thus requires a readout system that operates in a magnetic field. These requirements, and considerations of cost and engineering impact upon other detector subsystems and the accelerator, lead to the choice of a CsI(Tl) crystal calorimeter with photodiode readout. The relevant properties of CsI(Tl) are summarized in Table 7-2.

The radiation environment at PEP-II is more severe than that at existing e^+e^- colliders because of much higher beam currents. Given the radiation hardness of CsI crystals, the calculated background rates during luminosity running, discussed in Chapter 12, imply a wide safety margin. However, in actual storage ring operations, experience shows that most of the radiation exposure comes during beam injection and machine studies. Scaling typical CESR operation to the beam currents expected at PEP-II gives a radiation dose of about 1.5 krad/yr at a radius of 45 cm and 0.5 krad/yr at 100 cm [Blu86]. The PEP-II masking system has been designed with graded apertures to prevent the deposition of large amounts of radiation in the interaction region due to accidental beam loss. Nonetheless, it is desirable

Properties	CsI	CsI(Tl)	CsI(Na)
Radiation Length (cm)	1.86	1.86	1.86
Absorption Length (cm)	34.2	34.2	34.2
Light Yield (Photons/ MeV$\times 10^3$)	2–10	50–60	38–44
Light Yield Temperature Coef. (%/°C)	0.1	0.1	0.1
Molière Radius (cm)	3.8	3.8	3.8
Peak Emission (nm)	320	565	420
Lower Wavelength Cutoff (nm)	260	320	300
Refractive Index at Emission Maximum	1.95	1.79	1.84
Decay Time (ns)	10	940	630
Density (g/ cm^3)	4.51	4.51	4.51
Hygroscopic	slight	slight	weak

Table 7-2. *Properties of pure and doped CsI.*

to use detector components that are intrinsically radiation hard and can survive doses of tens of krad over the lifetime of the experiment.

7.2.2 Description of the Calorimeter

The baseline design of the CsI(Tl) calorimeter consists of a cylindrical barrel section and a forward conic endcap, as shown in Figure 7-4. Radially, the barrel is located outside the particle ID system and within the magnet cryostat. It weighs 24.2 metric tonne and is supported off each end of the coil at two points by eccentric pins. The barrel has an inner radius of 90 cm and an outer radius of 135.6 cm. It is located asymmetrically about the interaction point, extending, at its inner radius, 117.8 cm in the backward direction and 180.1 cm in the forward direction. The barrel covers a solid angle corresponding to $-0.80 \leq \cos\theta \leq 0.89$ in the laboratory frame (Figure 7-4).

The barrel is built out of 250 μm-thick carbon fiber composite (CFC) compartments that house individual crystals (Figure 7-5). At 90° to the beam, a compartment extends 43 cm radially. Aluminum support elements bonded to the back of each compartment allow them to be grouped into modules three crystals wide and seven crystals long, and to carry loads to a cylindrical strongback structure, which is fixed to the coil. By supporting the crystal at its rear, minimal material is placed in front of the crystals. The front material consists of

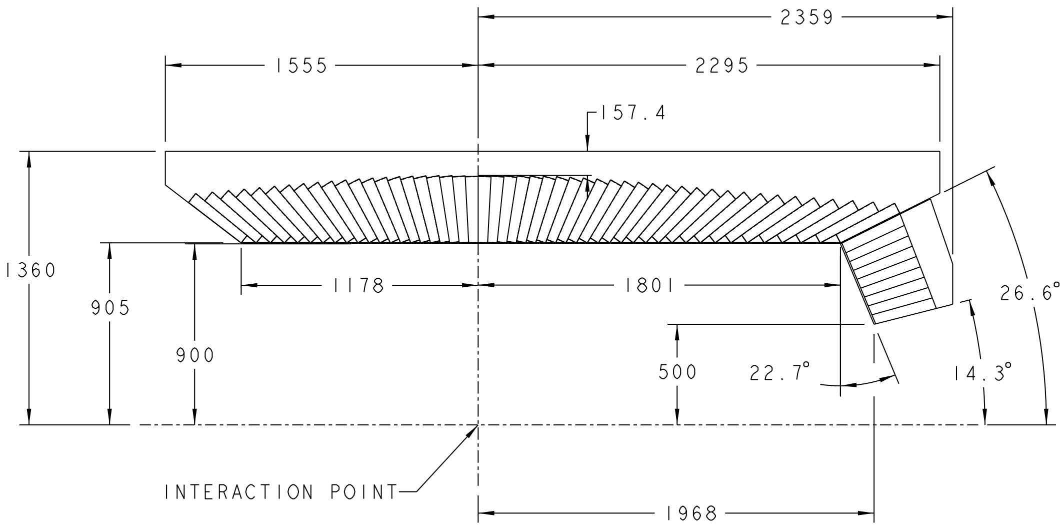

Figure 7-4. *Side view showing dimensions (in mm) of the calorimeter barrel and forward endcap.*

two 1 mm-thick cylinders of aluminum, separated by foam, which provide a gas seal and rf shielding; cooling, cables, and services are located at the back of each module.

The forward endcap is a conic section, with front and back surfaces tilted at 22.7° with respect to the vertical, which conforms to the drift chamber endplates, minimizing the distance to them. The endcap weighs about 4 metric tonne. It is supported off the coil rather than the flux return end doors, and is precisely aligned to the barrel to minimize the gap between the barrel and forward endcap. To further reduce the gap's effect on photon efficiency, it is nonprojective. The forward endcap starts at an inner radius of 50.0 cm from the beam line, making an angle of 250 mr with respect to the beam. It covers the solid angle from $\cos\theta = 0.97$ to $\cos\theta = 0.89$ in the lab.

The forward endcap is composed of two identical monolithic sections consisting of load-bearing outer containers filled with a honeycomb of 250 μm-thick CFC compartments, each containing one crystal package. The forward endcap is segmented vertically into two pieces, each of which can be retracted separately using a set of removable rails installed after the doors are opened. This allows fast access to the barrel end region.

Material in front of the calorimeter is kept to a minimum in order to achieve the required performance. In the barrel, the major source of such material is the DIRC ($\sim 0.18 X_0$). Including the beam pipe, the vertex detector, and the drift chamber, the total amount of material represents $\sim 0.23 X_0$ at normal incidence. The endplate of the drift chamber and the forward PID system contribute most of the material in front of the forward endcap. The endplate constitutes $\sim 0.065 X_0$. The aerogel represents an average of $\sim 0.095 X_0$. However,

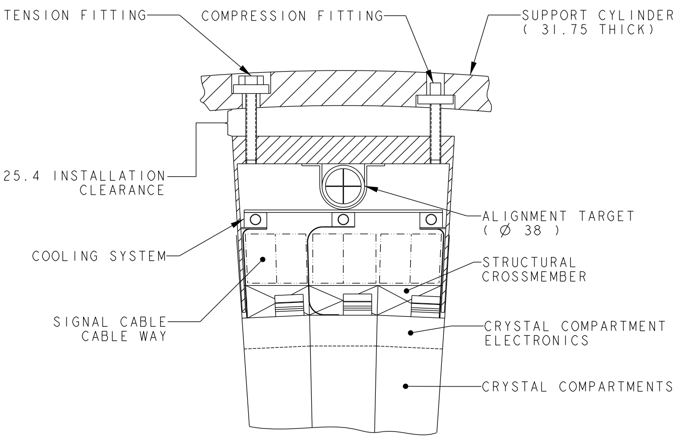

Figure 7-5. *Side view of typical barrel module and strongback.*

the ATC material is lumped: the aerogel itself represents $\sim 0.035X_0$, with the balance concentrated in the phototubes.

In both the barrel and endcap, each crystal is wrapped with a diffuse, reflecting material on its sides, with a reflector on its front face. Diode readouts and the preamplifier packages are located at the rear of each crystal box. Each crystal is held loosely in its box by a rear stiffening ring that also acts to locate and support the diode/preamplifier package. Cables for diode bias, preamplifier power and cooling, and calibration signals enter the back of the compartment. The crystal and electronics are shielded by a foil liner and a metal cap, respectively.

There are 5880 crystals in the barrel, arranged in 49 rows of distinct sizes, each having 120 identical crystals in azimuth. The forward endcap has a total of 900 crystals, made up from nine distinct radial rows $(3 \times 120, 3 \times 100, 3 \times 80)$ arranged to give approximately the same crystal dimensions everywhere.

The crystals are tapered along their length with trapezoidal cross sections. The average area of the front faces of the crystals is $4.8 \times 4.7\,\mathrm{cm}$, while the back face area is $6.1 \times 6.0\,\mathrm{cm}$. They vary in length in $0.5X_0$ steps from $17.5X_0$ in the forward part of the barrel to $16.0X_0$ in the backward part, with $17.5X_0$ in the forward endcap. The barrel and endcap have total crystal volumes of $5.2\,\mathrm{m}^3$ and $0.7\,\mathrm{m}^3$, respectively. Table 7-3 summarizes the crystal counts.

To minimize the loss of tracks that traverse inactive material between crystals, the crystals are arranged to be slightly nonprojective in θ with respect to the interaction point.

	Barrel	Forward Endcap
Number of Crystals ($17.5X_0$)	840	900
Number of Crystals ($17.0X_0$)	840	0
Number of Crystals ($16.5X_0$)	840	0
Number of Crystals ($16.0X_0$)	3360	0
Total Number of Crystals	5880	900
Total Volume (m^3)	5.2	0.7
Number of Crystals/Modules (ϕ)	120/40	120, 100, 80
Number of Crystals/Modules (θ)	49/7	9
Module Organization	$3_\phi \times 7_\theta$	Two C-sections

Table 7-3. *Summary of crystal counts and sizes in the barrel and endcap.*

7.2.3 Readout Chain and Trigger

The electronic readout chain is shown schematically in Figure 10-13 and described in detail in Chapter 10. Two independent photodiodes view the scintillation light from each crystal. Each diode has an independent dual-range preamplifier with calibration input. This two-fold redundancy is based on reliability issues presented in Section 7.4.4. Shaped, amplified signals are carried differentially to the end of the detector where they are input to ADCs which sample the data at a rate between 3 MHz and 5 MHz. The signals are digitized to an 18-bit effective dynamic range.

Digitized signals are passed out of the detector on fiber optic cables to the DAQ receiver modules, where calibration and waveform processing is performed. The data are then stored in video RAM. Trigger sums of $\sim$25 crystals are formed digitally on the DAQ cards. These data are passed along to the trigger for the full trigger decision.

The barrel digitization electronics is housed in 20 bays at the ends of the barrel. Forward endcap electronics is housed behind the endcap in six bays. Fiber optic cables are routed through channels between the barrel and endcap flux returns. Table 7-4 summarizes the channel organization and required space for the on-detector readout electronics.

	Barrel	Forward Endcap
Crystals	5880	900
Photodiodes	11760	1800
Preamplifier Boards	5880	900
Cables to ADC	11760	1800
Channels/ADC Board	25	25
ADC Boards/Bay	12	6
ADC Bays	20	6
Number of Fibers to DAQ (cm^2)	240 (4)	36 (1)

Table 7-4. *Summary of front-end electronics components.*

7.2.4 Review of Options

The baseline calorimeter has been described above. A number of variations have been evaluated, with some remaining under consideration. They are described briefly below.

Monolithic versus Modular Support System

Monolithic and modular support structures have been considered. Monolithic support structures, such as the CFC system used in the L3 BGO system, are fully integrated systems that combine strength and low mass. The major drawbacks to such assemblies are the increased complexity of fabrication and the high cost, arising in part from the need to incorporate proper compensation for the deformation of the structure when it is loaded.

Modular systems require more material to achieve the required strength and resistance to deformation. They are less expensive because each unit is small and hence easier to fabricate, handle, and assemble. Fabrication and assembly can occur at many locations simultaneously.

The *BaBar* calorimeter structure is a hybrid, with a modular system in the barrel and a monolithic system in the endcap. The relatively small size of the endcap should alleviate the problems of fabrication anticipated for a larger monolithic system, while reducing installation and access problems.

Longitudinal Segmentation of Crystals

Segmentation of crystals along their length (at about $3X_0$ from the front) to provide information on longitudinal shower development has been considered. Some improvement in e/π separation is indicated by Monte Carlo studies, but this is judged not to have a significant impact on the physics performance. Since the cost of implementation is prohibitive, this option is no longer being considered.

Crystal Cross Section: Trapezoidal Versus Hexagonal

While trapezoidal cross sections are conventional for crystal calorimeters, the use of hexagonal cross sections may offer certain advantages. In the endcap, an arrangement of hexagonal crystals on a spherical bounding surface can be designed that allows a single crystal size to be used, eliminating the problems associated with progressively smaller crystals of trapezoidal cross section and with abrupt transitions across superlayer boundaries.

Laboratory measurements indicate that for hexagonal crystals, about 25% more light is collected than for trapezoidal crystals. The response along the crystal is also more uniform [Jes94]. This might allow the acceptance criteria for crystal light yield and uniformity to be relaxed, leading to decreased costs. The crystal cost depends on the growth technique adopted; this is lower in some cases for hexagonal crystal shapes. However, the decreased growing cost is largely balanced by the increased cost of cutting and polishing six side surfaces instead of four.

Engineering design considerations make the cost and complexity of the support structures for hexagonal crystals greater than those for trapezoidal crystals. Complications also arise with hexagonal crystals at the interface of the barrel with the forward endcap, where it is vital to minimize gaps and inactive material.

Overall, we have not been convinced of any cost advantage in using hexagonal crystals. Therefore, trapezoidal crystals have been adopted in the baseline design for both barrel and endcap. The study of hexagonal crystals for use in the endcap will continue, subject to physics, engineering, and cost considerations, since the endcap is not on the same critical path as the barrel.

Direct Photodiode Versus Wavelength Shifter/Photodiode Readout

Two options for light collection and readout are presently under study. They are large area photodiodes directly attached to the crystal back face, and smaller-area photodiodes affixed to the edges of a wavelength-shifting plastic plate covering the crystal back face. Both techniques have produced results consistent with the desired noise performance. The cost, reliability, and reproducibility of each method are currently being evaluated (Section 7.4.1).

7.3 Projected Calorimeter Performance

7.3.1 Contributions to Photon Resolution and Efficiency

A number of effects beyond shower statistics contribute to the calorimeter resolution, with different effects dominating in different energy regions. Some of these contributions are linked, in that reducing the effect of one may facilitate improving another. The effects include:

1. Fluctuations in energy loss caused by leakage out of the front and the rear, by losses out the side due to the staggered geometry, and by losses in the inter-crystal material.
2. Fluctuations in transverse energy spread, with cluster sizes optimized to include effects of noise and background.
3. Scintillation light collection efficiency.
4. Light collection nonuniformity, coupled to fluctuations in shower position.
5. Incoherent electronic noise in the readout device.
6. Coherent noise and pickup.
7. Digitizer resolution.
8. Calibration of the energy scale, including crystal inter-calibration and the effects of time and temperature.
9. Material *en route* to the calorimeter. This affects efficiency as well as resolution.
10. Beam-related backgrounds.

In the high-energy regime, rear leakage (1) dominates the energy resolution. Fluctuations in energy loss (1), along with contributions from nonuniform light collection and calibration uncertainties (4) and (8), are expected to yield the constant term shown in Equation (7.1). Transverse shower spread and choice of reconstruction algorithms (2) also contribute at high energy, but become especially important to the energy resolution in the intermediate-energy range.

The low-energy regime is characterized by the importance of noise (5) and (6), and of beam-related backgrounds (10). Such backgrounds, especially if well above nominal levels, can also indirectly affect resolution through the need to reduce the number of crystals summed into a cluster, or the need to reduce the shaping time for the readout from the optimal value for maximizing the signal-to-electronic-noise ratio. Electronic noise is determined by the properties of the photodiode and preamplifier/shaper. Its value in units of energy is inversely proportional to the amount of light collected per unit of energy deposited (3).

Photon efficiency is primarily affected by the amount and distribution of material in front of the calorimeter (9), *i.e.,* in other detector systems, and also by losses (1) due to geometric edge effects.

Photon angular resolution is given by position resolution divided by the distance to the interaction point. Even for the best possible algorithm, fluctuations in shower shape (transverse energy spread) will limit the position resolution. The transverse crystal size at the rear should be less than two Molière radii, but returns diminish when that size is comparable to a Molière radius.

Contribution to Energy Resolution from Crystal Nonuniformity

The effect of nonuniform light output along a CsI crystal has been studied using a stand-alone GEANT simulation. An untapered, 35 cm-long crystal with large lateral dimensions ($40 \times 40\,\mathrm{cm}$) is divided along its length into 100 slices. A nonuniform response is imposed as a weight on the energy deposited in the slices for each event.

A study of linearly decreasing and increasing efficiencies for light collection along the crystal for photon energies between 200 MeV and 9 GeV has been done. The contribution to the energy resolution σ_E/E due to crystal nonuniformity is shown in Figure 7-6(a) for three different linearly decreasing weight functions (10%, 5%, and 2.5% over the full length of 35 cm). Nonuniformities with decreases up to 5% over the full crystal length lead to an energy resolution contribution which meets the requirement stated in Section 7.1.2.

Linearly increasing weight functions lead to changes in the energy resolution that cannot be presented in the same way; for photon energies above 1 GeV the energy resolution improves. Figure 7-6(b) shows the resolution σ_E/E as a function of the increase over 35 cm. The result for higher energies can be understood as a compensation for leakage of the electromagnetic shower at the rear end of the crystal. A similar behavior has been observed in a Monte Carlo study for the CLEO-II calorimeter [Blu86].

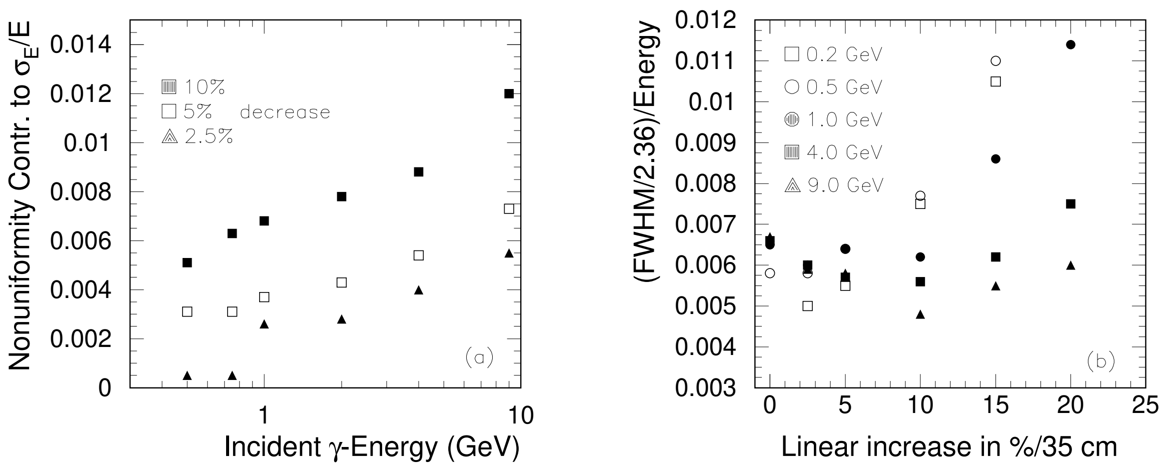

Figure 7-6. *Energy resolution for nonuniform light output along a CsI crystal of 35 cm length. (a) Contribution to σ_E/E from light output decreasing towards the crystal end (2.5%, 5%, 10% over the crystal length). (b) σ_E/E for light output increasing towards the crystal end. Note that the crystal dimensions used for this study are much larger than baseline lengths and transverse leakage is ignored.*

Contribution to Energy Resolution from Beam Backgrounds

Simulations indicate that beam-related background is almost entirely caused by beam-gas interactions or by off-axis beam particles striking machine elements near the interaction region. Synchrotron radiation photons are a negligible source of background [Zis91]. The energy distribution of the shower remnant photons has a median of ~500 keV. About 311 depositions per microsecond with a total energy of 0.33 GeV are expected in the barrel, while in the forward endcap, about 20 depositions per microsecond with a total energy of 0.07 GeV are expected. There are on average 0.7 (0.4) depositions per microsecond above 20 MeV in the barrel (forward endcap) that can produce fake photons in reconstructed events. The effect of beam backgrounds on photon energy resolution has been studied. Lost particle backgrounds corresponding to 1 times nominal and 10 times nominal levels in 1 μs windows were generated together with 100 MeV photons in the barrel and forward endcap. Comparison with the zero background case shows contributions, in quadrature, to the resolution σ = FWHM/2.36 of 0.55 MeV from 1 times nominal background and 1.05 MeV from 10 times nominal background (*i.e.,* 0.55% and 1.05%, respectively, at 100 MeV).

7.3.2 Modeling

The expected calorimeter performance has been studied using a GEANT Monte Carlo simulation of the full detector. The GEANT model of the calorimeter contains a description of the barrel with crystal lengths varying in $0.5X_0$ steps from $17.5X_0$ in the forward part to $16X_0$ in the backward part, with $17.5X_0$ crystals in the forward endcap. The model includes $500\,\mu$m of carbon fiber composite as structural material between the crystals and a 5 mm gap at the barrel/forward endcap interface.

The full detector model includes a DIRC particle ID device in the barrel and an aerogel device in the forward endcap. They are modeled according to the description given in Chapter 2. The DIRC represents about $0.18X_0$ at normal incidence. Together with the beam pipe, the silicon vertex detector, and the drift chamber, this totals $0.23X_0$ in the barrel region at normal incidence. In the forward region, the materials incorporated in the detector model, as represented in Figure 2-16, is different from that described in the balance of the Technical Design Report. Thus, in the forward region, material in front of the endcap calorimeter totals about $0.35X_0$.

Photons are reconstructed by forming clusters of contiguous crystals with energies above 0.5 MeV. In studies of the performance for single photons, their energies are determined by summing up the energy deposited in an area corresponding to 5×5 crystals at $90°$. In studies involving π^0s, the cluster energy is determined as the sum of the energies of all contiguous crystals making up the cluster. To deal with overlapping showers, the cluster is searched for additional local energy maxima, which are then treated as seeds for subclusters. The subcluster energies are determined in an iterative way by dividing up the energy in shared crystals according to the seed energy as it develops and adding it to the seed. In both methods, an incoherent electronic noise contribution of 150 keV per crystal is included. Since the distribution of deposited energy typically shows a non-Gaussian tail on the low side, the resolution is defined as $\sigma = \mathrm{FWHM}/2.36$. In order to allow for effects not included in the GEANT simulation, such as nonuniform light collection and calibration uncertainties, 0.5% is added in quadrature to σ_E/E.

Efficiency for single photons is defined as the fraction of events with a ratio of measured over generated photon energy, $R = E/E_0$, above an E_0-dependent cut value:

$$RCUT(E_0) = 1 - 0.05 \times \frac{\sigma_E/E(E_0)}{\sigma_E/E(E_0^{max})} \;, \tag{7.3}$$

where $\sigma_E/E(E_0)$ is the target energy resolution (Equation 7.1) at energy E_0, and $E_0^{max} =$ 5 GeV; therefore, $RCUT(5\,\mathrm{GeV}) = 0.95$, and $RCUT(100\,\mathrm{MeV}) = 0.92$. (Note that in calculating R, the measured photon energy distribution has been calibrated so that its peak value equals E_0.)

7.3.3 Expected Performance for Photons

Initially, the performance of the calorimeter has been studied without any material in front of it. Figure 7-7 shows energy resolution and efficiency, as defined above, *vs.* energy, for single photons with polar angles near 90°. Also shown (solid line) is the target energy resolution (Equation 7.1). The predicted resolution, based on $16.5X_0$ crystals near 90°, is just above the target resolution. The sawtooth crystal layout at the inner radius of the barrel calorimeter causes some performance degradation towards small polar angles. Figure 7-8 shows energy resolution and efficiency *vs.* polar angle for photons with energies of 100 MeV and 1 GeV. One can see a 40% (20%) worsening of resolution for 100 MeV (1 GeV) photons at $\cos\theta$ values near the end of the barrel. This effect is due to increased leakage, mostly out of the uncovered crystal side faces. This degradation is probably acceptable over the limited solid angle involved. (It could be ameliorated by decreasing the crystals' transverse dimensions (front-side leakage) and increasing their length (rear-side leakage). Studies have shown that simply filling in the sawtooth pattern degrades efficiency and uniformity of light collection significantly [Spi94]).

A photon that converts in the material between the main tracking volume and the calorimeter can either be lost entirely or so degraded that it will fail to lead to a satisfactory π^0 mass. While energy loss by the conversion e^+ and e^- is a contributing factor, even more important is their deflection by the solenoidal field, so that one or both of the leptons may not reach the barrel calorimeter. For the endcap, in contrast, the conversion leptons will spiral around the field lines and eventually reach the calorimeter close to the intersection point of the projected photon. Important considerations besides the amount of material traversed include the proximity of that material to the calorimeter and whether the particle ID detector can "flag" the conversion [Eis93]. The effect of material in front of the calorimeter has been simulated using the full GEANT model of all detector systems. The results for energy resolution and efficiency are shown in Figure 7-9. Note that there is only a small effect on resolution since most photons pass through the material unaffected. However, those that interact experience a significant energy loss, resulting in a reduction in efficiency of 2-32% at 100 MeV and 6-12% at 1 GeV, depending on $\cos\theta$. More details can be found in Reference [BaB94]; the effect on π^0 reconstruction is presented below.

The detailed reconstruction algorithms needed to determine the positions of showers are still being developed. A crude algorithm being used at the moment is based on a corrected energy-weighted center-of-gravity method. Due to the finite granularity of the calorimeter, the resulting shower positions are biased towards the crystal centers. A correction, derived from Monte Carlo, is applied in an attempt to remove this bias. The resulting resolution in polar angle θ is shown in Figure 7-10 as a function of energy, together with a parameterization of the CLEO-II angular resolution. It is slightly better than the CLEO-II resolution, as a result of our lower electronic noise, smaller transverse crystal sizes, and longer distances to

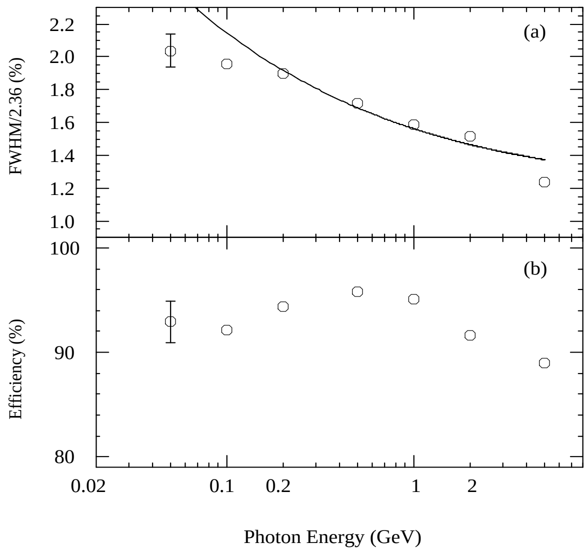

Figure 7-7. *(a) Energy resolution and (b) efficiency (as defined in the text) vs. energy for photons with polar angles near 90° and 16.5X_0 crystals without any material in front of the calorimeter. The solid line shows the target resolution (Equation 7.1).*

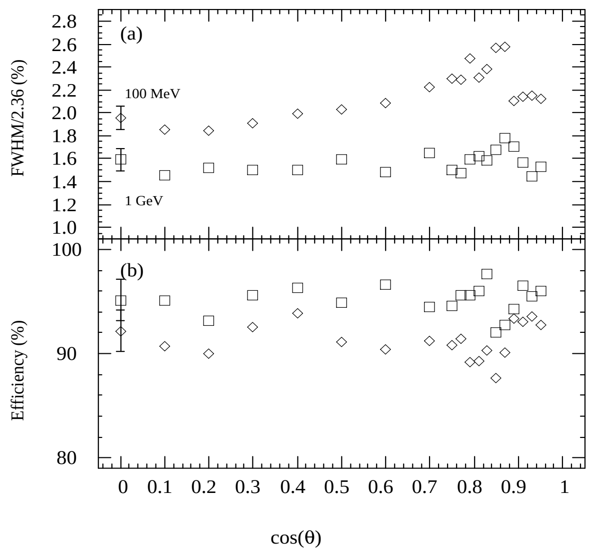

Figure 7-8. *(a) Energy resolution and (b) efficiency vs.* $\cos\theta_{cm}$ *for 100 MeV and 1 GeV photons without any material in front of the calorimeter.*

many of the crystals. Figure 7-11 shows θ resolution *vs.* polar angle for different photon energies. Note that the angular resolution is comparable for showers in the barrel and in the endcap since, in contrast to the case at CLEO, the endcap crystals are also arranged in quasi-projective geometry.

7.3.4 Expected Performance for π^0s

Most photons detected in the calorimeter arise from π^0s. To study π^0 mass resolution and efficiency and the effect of material in front of the calorimeter, single, monoenergetic π^0s have been simulated using the GEANT model of the full detector. Figure 7-12 shows π^0 mass resolution and efficiency *vs.* π^0 momentum for π^0s with $\cos\theta_{cm} = 0$. Mass resolution is again defined as $\sigma = \mathrm{FWHM}/2.36$; efficiency is obtained using a $\pm 3\sigma$ cut around the π^0 mass. Also indicated is the performance without any material in front for π^0 momenta of 100 MeV/c and 1 GeV/c. As is the case for single photons, the inactive material has very little effect on the resolution, but significantly degrades the efficiency.

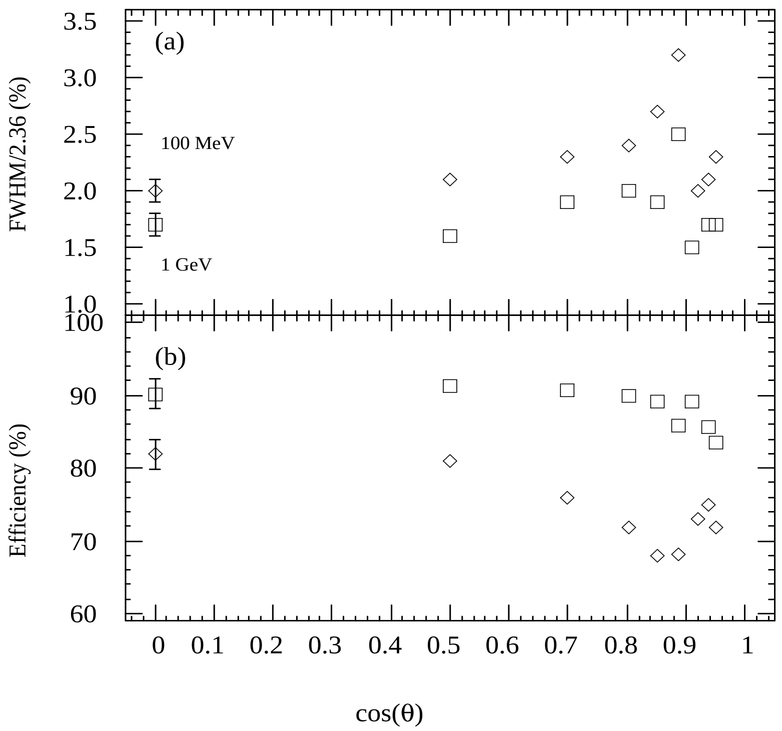

Figure 7-9. *(a) Energy resolution and (b) efficiency for 100 MeV and 1 GeV photons vs. polar angle with the full detector model.*

In addition, several benchmark processes relevant for measuring *CP* asymmetries have been used to study π^0 mass resolution and efficiency: $B^0 \to J/\psi\, K^{*0}$, $K^{*0} \to K^0_S\pi^0$; $B^0 \to \rho^\pm\pi^\mp$, $\rho^\pm \to \pi^\pm\pi^0$; and $B^0 \to \pi^0\pi^0$. The π^0s from those processes cover a wide range of momentum, with $B^0 \to J/\psi\, K^{*0}$ yielding the softest π^0s and $B^0 \to \pi^0\pi^0$ the hardest. Figure 7-13(a) shows the $\gamma\gamma$ invariant mass spectrum in the decay $B^0 \to J/\psi\, K^{*0}$, with no material in front of the calorimeter. (Note that the K^0_S is not allowed to decay to $\pi^0\pi^0$ in this study, and the J/ψ decays into lepton pairs only.) The π^0 mass resolution and efficiency are $\sigma_{m_{\pi^0}} = 4.0\,\mathrm{MeV}/c^2$ and 74%, respectively. Also shown (Figure 7-13(b)) is the mass spectrum when the detector material is included in front. Again, the additional material leads to a relatively small degradation in resolution to $\sigma_{m_{\pi^0}} = 4.5\,\mathrm{MeV}/c^2$, but causes a very significant low-mass tail which results in a drop in efficiency to 59%. The results for all three channels are summarized in Table 7-5.

In the all-neutral channel $B^0 \to \pi^0\pi^0$, we achieve a B^0 mass resolution of $\sigma_{m_B} = 62\,\mathrm{MeV}/c^2$ (Figure 7-15) and an overall reconstruction efficiency of 62%, using a π^0-mass cut of $110 \leq m_{\gamma\gamma} \leq 160$ MeV/c^2 and a B-meson mass cut of $5000 < m_{\pi^0\pi^0} < 5350$ MeV/c^2(Figure 7-14).

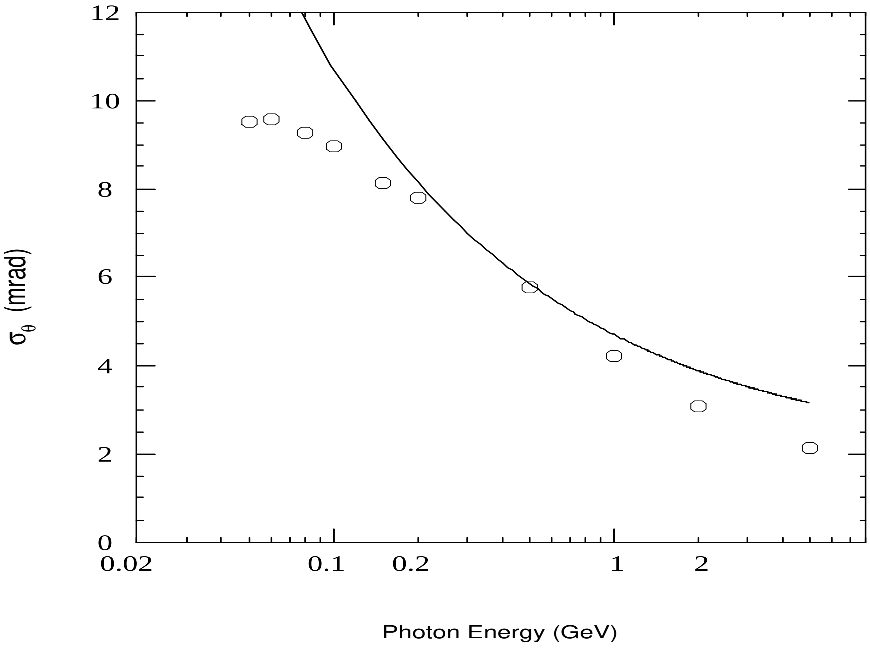

Figure 7-10. *Resolution in polar angle vs. energy for photons with polar angels near 90°. The solid line shows a parameterization of the measured CLEO-II resolution in the barrel.*

B Decay Channel	$\sigma_{m_{\pi^0}}$ (MeV/c^2)	Efficiency (%)
$B^0 \rightarrow J/\psi\, K^{*0}$	4.5	59
$B^0 \rightarrow \rho^{\pm}\pi^{\mp}$	5.5	65
$B^0 \rightarrow \pi^0\pi^0$	8.3	72

Table 7-5. *π^0 mass resolution and efficiency in various B decay channels, modeled with the complete detector material in front of the calorimeter.*

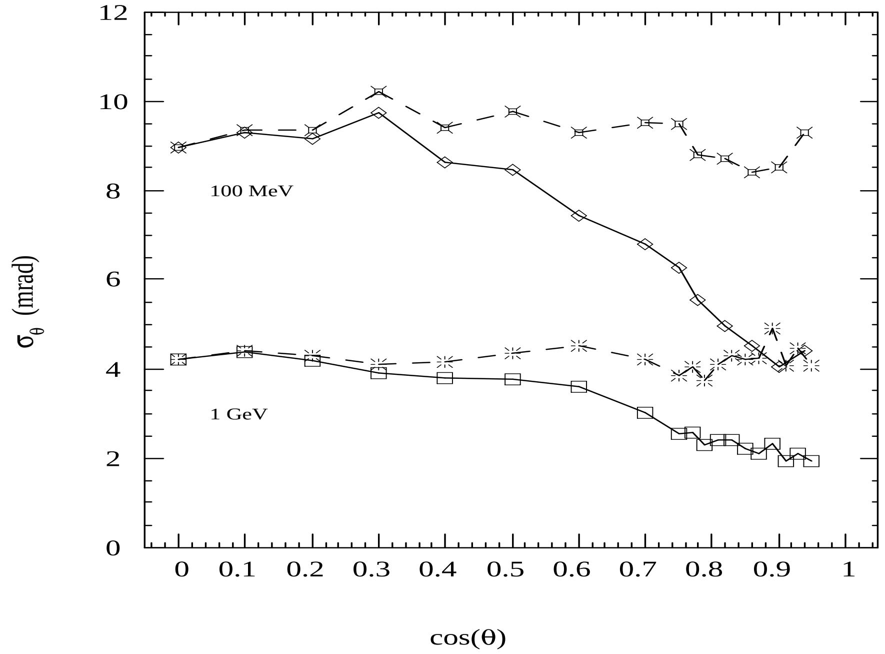

Figure 7-11. *Resolution in polar angle vs. polar angle for 100 MeV and 1 GeV photons. The points connected by the dashed lines show the resolution with the distance effect removed.*

7.3.5 e/π Separation

In the *BaBar* calorimeter, electrons are totally absorbed, while muons and some pions, having momenta above a few hundred MeV/c, penetrate to the Instrumented Flux Return (IFR), depositing only a fraction of their energy.

Since the drift chamber provides a precise momentum measurement, electrons can be identified using energy-momentum matching. In addition, electromagnetic showers are usually narrower than hadronic showers, so the lateral shower profile can be used to further distinguish electrons from pions. The results of such a study [Zhu95] using a GEANT simulation of the detector, with electrons of momenta in the range 500 MeV/c to 5 GeV/c produced at polar angles of 90°, indicate that the probability of misidentifying a pion as an electron is $\sim 10^{-3}$ for an electron efficiency of $\sim$95% (Table 7-6).

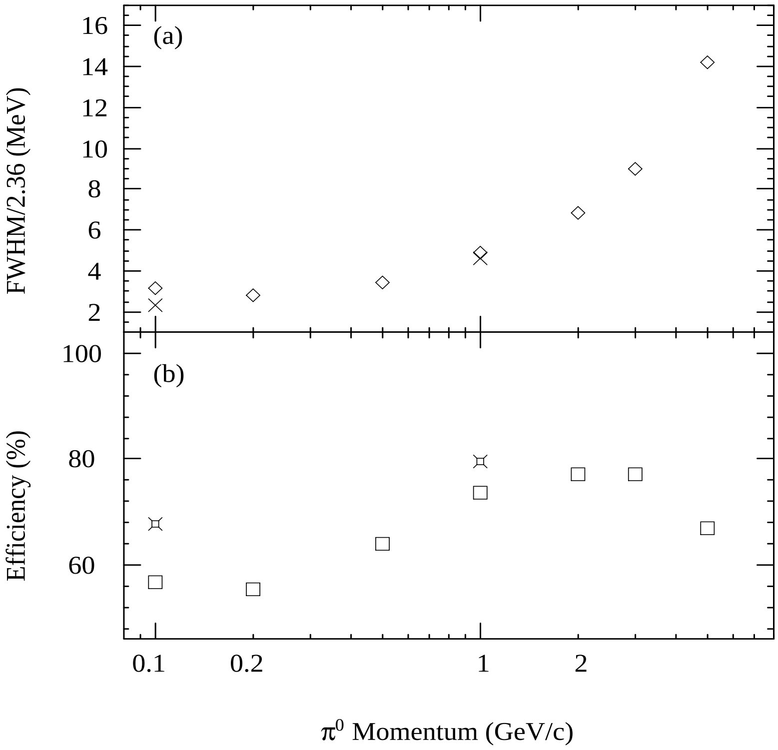

Figure 7-12. *(a) Mass resolution and (b) efficiency (as defined in the text) for single, mono-energetic π^0s vs. π^0 momentum with the full detector model (π^0s are generated with $\cos\theta_{cm} = 0$). The crosses indicate the performance for 100 MeV/c and 1 GeV/c π^0s with no material in front of the calorimeter.*

Momentum	Events	Electron	π^+	π^-
	Generated	1000	5000	5000
0.5 GeV/c	Surviving	926	3	7
1.0 GeV/c		968	1	1
5.0 GeV/c		972	0	1

Table 7-6. *Results of a GEANT study of e/π separation.*

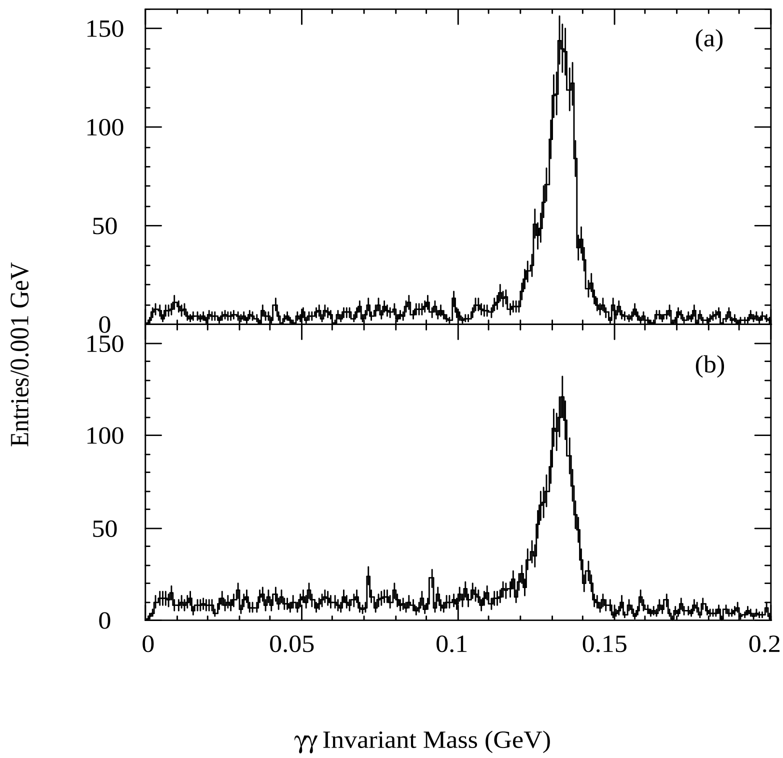

Figure 7-13. *$\gamma\gamma$ invariant mass distribution in the process $B^0 \rightarrow J/\psi\, K^{*0}$, $K^{*0} \rightarrow K^0_S\pi^0$, $K^0_S \rightarrow \pi^+\pi^-$ for (a) no material in front of the calorimeter and (b) the full detector model.*

7.3.6 Performance and Cost Optimization

Taking into account the correlation between maximal photon energy and polar angle caused by the boost of the center-of-mass system, crystal lengths can be varied as a function of polar angle without significantly affecting the calorimeter performance in *CP*-relevant B decay modes. The process $B^0 \rightarrow \pi^0\pi^0$ has been used as a benchmark. Crystal lengths are chosen to keep the corresponding energy resolution (Figure 7-16) close to the target resolution at all polar angles. This mode has also been used to check the effect of shorter crystals on the B mass resolution. For a calorimeter in which all crystals are shortened by $1X_0$, one obtains $\sigma_{m_B} = 73\,\mathrm{MeV}/c^2$ and an overall reconstruction efficiency of 57%. Such a performance is significantly worse than that of the baseline design.

Using the center-of-gravity method described above, angular resolution has been studied as a function of transverse crystal size (see Figure 7-17). One finds a rather weak dependence, especially at high energies where there is significant energy sharing between the crystals in

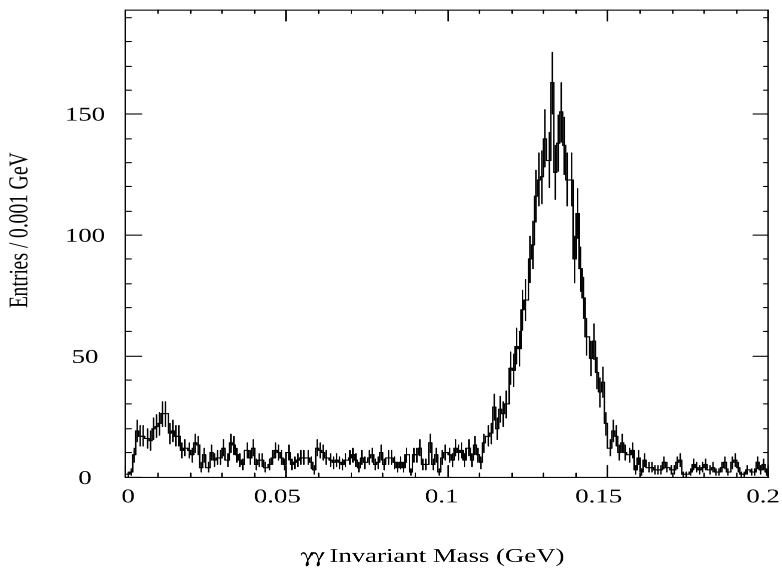

Figure 7-14. *$\gamma\gamma$ invariant mass distribution in the process $B^0 \to \pi^0\pi^0$, using the full detector model.*

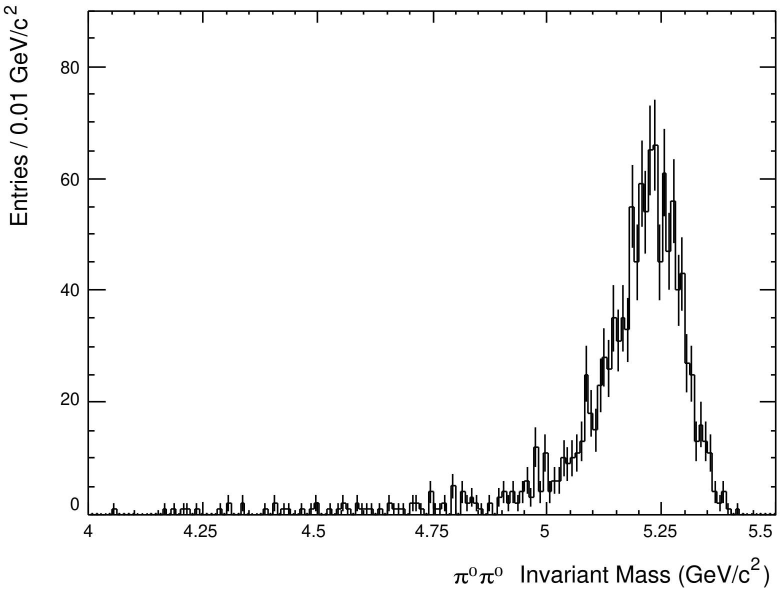

Figure 7-15. *$\pi^0\pi^0$ invariant mass distribution where $110 < m_{\gamma\gamma} < 160\,MeV/c^2$, in the process $B^0 \to \pi^0\pi^0$, using the full detector model.*

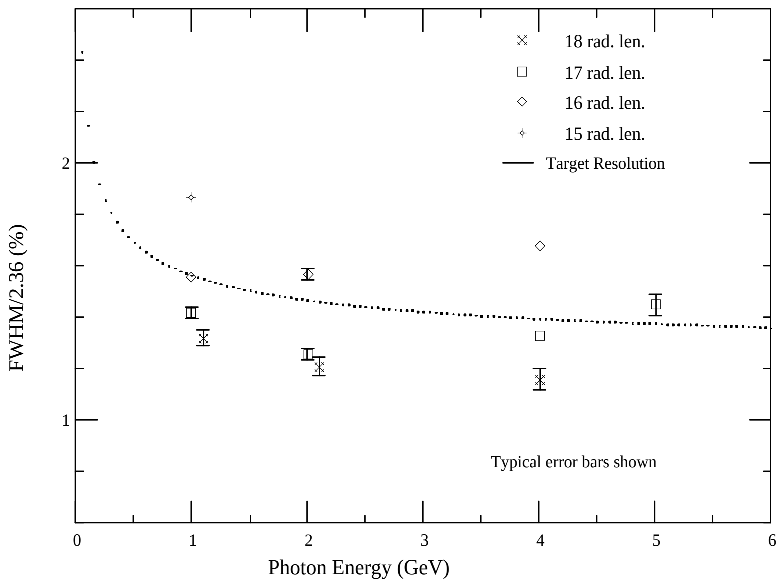

Figure 7-16. *Energy resolution vs. energy for a number of crystal lengths and for photons with polar angle near 90°. The solid line shows the target resolution (Equation 7.1).*

Material Thickness	σ_E/E (%)	Efficiency (%)
0 μm	1.6	82
500 μm	2.1	79
800 μm	2.3	78

Table 7-7. *Energy resolution and efficiency for 100 MeV photons with* $\cos\theta_{cm} = 0$ *for different thicknesses of the inter-crystal material.*

the cluster. The angular resolution for our choice of transverse crystal size is consistent with the target (Equation 7.2).

The effect of the CFC structural material and crystal wrappings on energy resolution and efficiency is given in Table 7-7 for photons with energies of 100 MeV and polar angles around 60°. Note that the baseline design has an amount of inter-crystal material equivalent to about 800 μm of CFC. As can be seen, the performance degrades slowly for material thicknesses greater than 500 μm of CFC equivalent.

Making the inter-crystal cracks nonprojective does not help with the loss of resolution shown in Table 7-7, but it does allow recovery of much of the lost efficiency. This has been studied in detail for the 800 μm case. In both θ and ϕ, most of the loss is recovered with a nonprojective angle of 15 mr (about 6 times the angle subtended by the crack). The baseline design includes

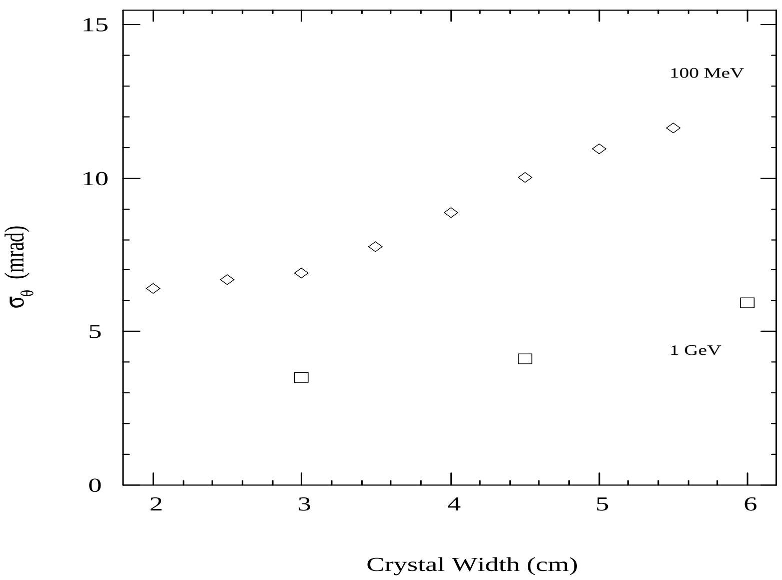

Figure 7-17. *Resolution in polar angle vs. transverse crystal size for 100 MeV and 1 GeV photons.*

15 mr of nonprojectivity in θ only, and relies on misalignment to produce a smaller amount of nonprojectivity in ϕ. Even without the latter, the photon efficiencies are within 2% of the zero-material values; this loss is small compared to that resulting from material in front of the calorimeter.

7.4 Crystal Subassemblies and Readout

A crystal subassembly consists of a CsI(Tl) crystal covered with a suitable reflective material wrapped in a thin aluminum foil and a readout package located at the rear. The readout package consists of silicon PIN photodiodes closely coupled to low-noise, charge-sensitive preamplifiers, both enclosed in a metal cap. (The exact crystal dimensions are given in Section 7.6; for a detailed description of the front-end electronics refer to Chapter 10.) All components are selected to have a uniform and high level of light collection, together with minimal noise contribution from the readout electronics, in order to achieve optimal energy resolution.

7.4.1 Photodiode Readout

Signal-to-Noise Considerations

The requirement for the readout system is that at the lowest photon energies of interest (~20 MeV), the electronic noise must not dominate the resolution. In the absence of electronic noise, the resolution at these energies is expected to be on the order of 500 keV, mostly due to shower leakage fluctuations. The electronic noise contribution to the cluster energy resolution is required to be smaller than 500 keV. This results in an upper limit of about 150 keV per crystal, assuming that less than a dozen crystals are summed into a cluster at such low photon energies.

Electronic noise has two components, an incoherent one which derives from thermal and shot noise in the readout, and a coherent one which comes predominantly from pickup. Experiments using arrays of CsI(Tl) similar to the one proposed here have achieved incoherent noise performances of 250–500 keV per crystal at room temperature [Ake92, Kub92]. Noise performance at the 150 keV/crystal level should be achievable with improvements in average crystal light output, surface preparation, light collection, photodiode packaging, low-noise charge-sensitive preamplifiers, and shaper amplifiers. A target at this level has been set for the readout system. This meets the resolution requirements and allows the use of radioactive γ sources for crystal monitoring (with beams off). Note that lower noise per crystal implies improved energy resolution because a larger number of crystals per shower can be summed.

Shielding is needed for protection against coherent pickup noise. The entire calorimeter is enclosed in a metallic Faraday housing. The crystal housings are metallized to reduce cross coupling, and the diode-to-preamplifier connection uses shielded cable of minimum length. Both the diode and the preamplifier are encapsulated in a metal cap for electromagnetic shielding.

The equivalent electronic noise energy (ENE) for a crystal with a given readout system can be calculated as

$$\mathrm{ENE} = \frac{\mathrm{ENC}}{L(pe/\,\mathrm{MeV})} \,, \tag{7.4}$$

where ENC is the equivalent noise charge in number of electrons, and $L(pe/\,\mathrm{MeV})$ is the light yield in electrons per MeV of energy deposition. Equation 7.4 indicates that achievement of low ENE requires not only low intrinsic noise of the electronics (ENC), but also a highly efficient photodetector coupled with maximal light output of the crystal. The resulting light yield requirements are detailed in Section 7.4.3.

Each crystal is read out by two independent photodiode-preamplifier-shaper channels [Hal95]. The two channels are then summed before digitization. The redundancy is due to reliability requirements (Section 7.4.4), and the noise per crystal is the incoherent sum of the noise of the two channels.

The principal contributions to the electronic noise are the shot noise from the dark current of the diode and the thermal noise of the preamplifier [Gro84]. The shaping time affects the relative contributions of the two components. Two possible readout schemes, one using two Hamamatsu S3588-03 photodiodes ($3.4 \times 30\,\mathrm{mm}^2$ active area) mounted on a wavelength shifter (WLS) and the other using two Hamamatsu S2744-03 photodiodes ($10 \times 20\,\mathrm{mm}^2$ active area) directly affixed to the crystal, are being considered. A preamplifier-shaper hybrid for both options has been developed and tested. The equivalent noise charge per crystal for the WLS option is 620 e^- and for the direct option 680 e^-, using a $2\,\mu$s shaping time [Jes95a]. Note that a slight cooling of the diodes may further reduce the noise. The dark current of the photodiodes is halved by a reduction in temperature of as little as 5–7°C. Studies of noise *vs.* temperature are presently underway.

Wavelength Shifter/Photodiode Readout

Typical silicon PIN photodiodes (*e.g.,* Hamamatsu S 3588-03,S 2744-03) show a broad spectral response peaking at wavelengths around 960 nm. They have a quantum efficiency of about 75%. The photon spectrum of CsI(Tl), on the other hand, has its peak emission around 560 nm. In addition, there is an order of magnitude mismatch between the light-emitting area of the crystal and the sensitive area of the photodiode. Thus, the purpose of the WLS is twofold: to shift the wavelength of the CsI(Tl) scintillation light to the more sensitive range of the photodiode, and to work as a flux concentrator by collecting the light onto the sensitive area of small, relatively inexpensive photodiodes through total internal reflection.

Fluorescent dyes are suitable materials for wavelength shifters [Lor86]. They show a large difference in absorption and emission wavelengths and re-emit the fluorescent light isotropically. The absorption of the dye should match the emission of CsI(Tl), and the re-emission of fluorescent light must take place at wavelengths as long as possible, with good internal quantum efficiency, small luminescent decay time, and low light loss. The overlap of the absorption and re-emission spectra of the wavelength shifter should be minimal in order to prevent self-absorption of luminescent light.

Typical wavelength shifters consist of thin plastic tiles doped with dye concentrations of a few hundred ppm [Lor86, Fis87]. The dyes used so far (BBQ, Y7, BASF Lumogen F red 339) have Stokes shifts of only ~50 nm [Ake92, Kam83] and therefore show a large self-absorption of about 50% [Kei70]. Figure 7-18 shows the absorption and re-emission spectra of a wavelength shifter similar to that used by the Crystal Barrel [Ake92]. Transmission as high as 30% has been achieved with this material.

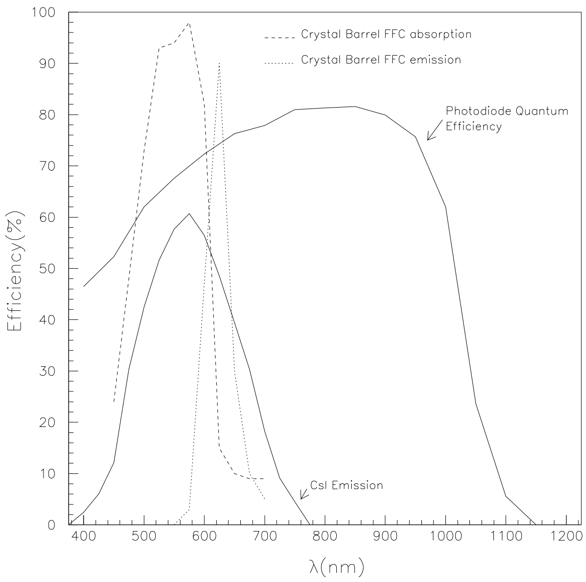

Figure 7-18. *Absorption and fluorescence re-emission spectra of the Crystal Barrel wavelength shifter using BASF Lumogen F red 339 dye. Overlayed are the emission spectrum of CsI(Tl) and the photosensitivity of the Hamamatsu S 3588 photodiode.*

Fluorescent dyes that are used for Nd:YAG pumped dye lasers (*e.g.,* Styryl 8, Styryl 9M) absorb around 550 nm, re-emit above 750 nm, and have nearly no self-absorption. Acrylic material, such as PMMA, is used to carry the dye. These dyes must, however, be dissolved in a polar co-polymer before adding to the PMMA. Whether these dyes have high enough quantum efficiency and the optimal concentration for high absorption and high quantum efficiency are being investigated.

Figure 7-19 shows the proposed WLS setup with two PIN diodes. The WLS covers almost the entire rear face of the crystal. The re-emitted light is concentrated along the WLS side faces by total internal reflection and read out using small-area rectangular photodiodes (*e.g.,* Hamamatsu S 3588-03, $30 \times 3.4\,\mathrm{mm}^2$). The diodes are attached to the WLS with Kodak HE-80 epoxy or Cargille Meltmount. The thickness of the WLS is primarily chosen to match the area of the photodiode. For redundancy, and in order to minimize light losses, two photodiodes are glued to two adjacent side faces of the WLS. To increase the light collection efficiency, a white diffuse reflector is placed behind the wavelength shifter, with an air gap to maintain total internal reflection inside the WLS. The other edges are polished and coated with white diffuse reflecting paint.

The light yield for a variety of crystals has been measured with the WLS/diode option [Jes95a]. For an $18X_0$ tapered crystal with a front face $4.5\times4.5\,\mathrm{cm}^2$ and rear face $5.8\times5.8\,\mathrm{cm}^2$, wrapped in three layers of $38\,\mu$m-thick Teflon, a light yield of 4600 $pe/$ MeV has been measured. The

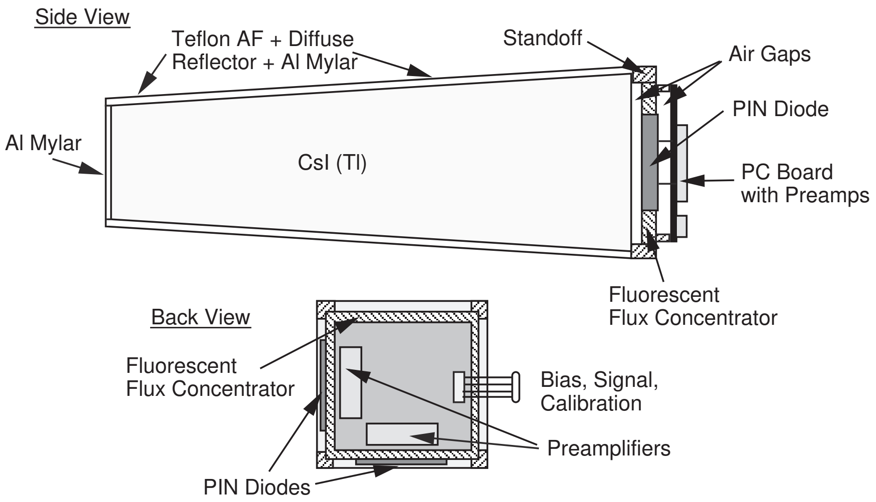

Figure 7-19. *CsI(Tl) readout assembly (not to scale).*

equivalent noise charge for the two diodes combined is 620 e^-, which implies an equivalent noise energy of 135 keV per crystal. For comparison, the Crystal Barrel Collaboration has achieved an equivalent noise energy of 220 keV with a similar wavelength shifter geometry and one diode [Ake92].

Tests of possible radiation damage or aging effects of the WLS and the epoxy used for the WLS/photodiode bond must be completed. Radiation damage tests will be carried out using ^{60}Co sources. There will also be long-term tests at normal and elevated temperatures.

Direct Photodiode Readout

Photodiodes can, alternatively, be placed directly on the back of the CsI(Tl) crystal. To collect a sufficient amount of scintillation light, two large-area photodiodes (*e.g.,* Hamamatsu S 2744-03, $10 \times 20\,\mathrm{mm}^2$) must be used. The balance of the back surface is covered with a diffuse reflector. This technique is more sensitive than the WLS readout to variations in light production and collection because the back surface is not fully covered by detectors. Direct readout with four small-area (Hamamatsu S 1723, $10 \times 10\,\mathrm{mm}^2$) photodiodes is used in the CLEO-II calorimeter, which yields an equivalent noise energy of 500 keV [Kub92].

A variety of crystals have been measured using two Hamamatsu S2744-03 ($20 \times 10\,\mathrm{mm}^2$) diodes [Jes95a]. Using the same $18X_0$ crystal as in the WLS test previously described, we measure a light yield of 5960 $pe/$MeV. The equivalent noise charge of the two diodes combined is 680 e^- to give an equivalent noise energy of 114 keV per crystal. For comparison, the BELLE Collaboration has achieved 150 keV in similar tests [BEL94].

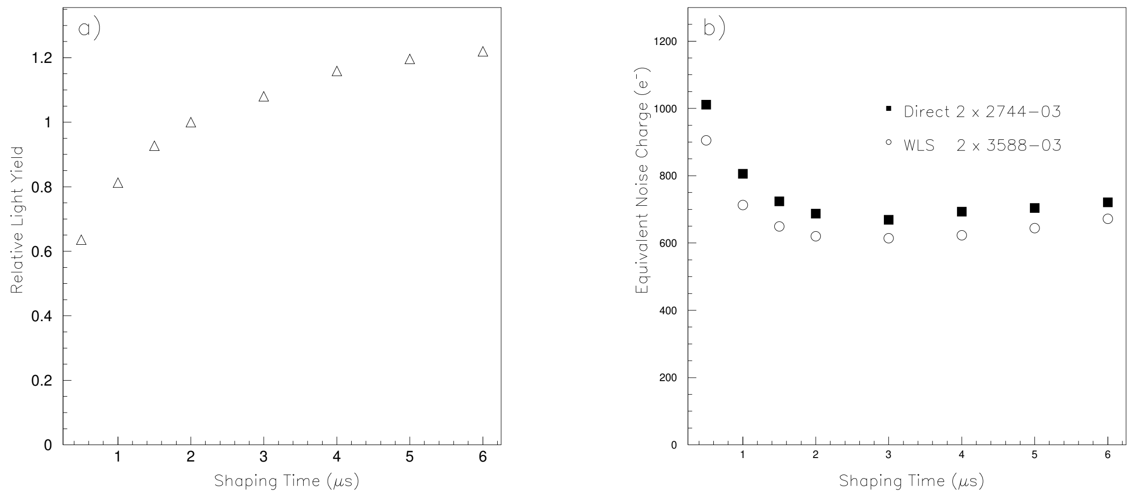

Figure 7-20. *(a) Relative light yield vs. shaping time and (b) noise vs. shaping time for the direct and WLS readout schemes.*

Conclusions

In bench tests, the WLS and direct readout options have achieved comparable performance. Further improvements in performance are anticipated with new WLS dyes and diode cooling. Once noise equivalents of about 150 keV per crystal using WLS readout are routinely achieved, this solution will be adopted. The overall complexity and reliability of such a readout system is comparable to that of direct diode coupling but has the advantage of substantially lower cost.

Note that all tests used a shaping time of $2\,\mu$s. A lower value may be needed in order to reduce beam-related backgrounds [Lev94]. Figure 7-20 shows how to scale the light yield and noise for different values of the shaping time.

7.4.2 Light Collection

Surface Preparation, Wrapping, Coating, and Tuning

Each crystal is cut and polished by the manufacturer. The light output of the crystal is required to be uniform along its length. This is traditionally accomplished by roughening the crystal surface selectively to reduce locally the reflected light and then wrapping the crystal in multiple layers of a suitable reflector, such as PTFE Teflon. The highest light yield is obtained by the use of a high-reflectivity white diffuse reflector with a small airgap

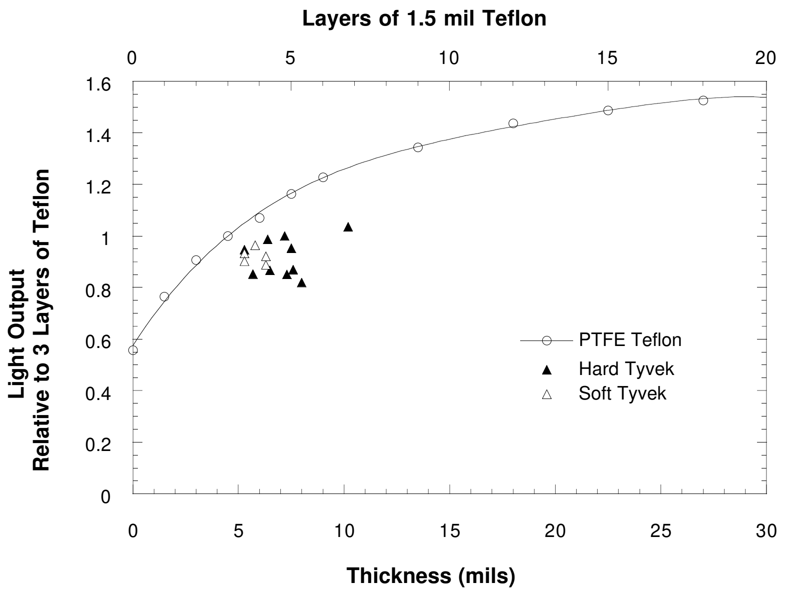

Figure 7-21. *Light output vs. number of layers of PTFE Teflon and DuPont Tyvek. (In each case, there is one cover layer of aluminum foil.)*

between the reflector and the crystal surface. The light yield increases with the number of Teflon layers used to wrap the crystal (Figure 7-21).

One potential wrapping scheme for the crystals uses four layers of PTFE Teflon, each layer being $38 \pm 5\,\mu$m thick. This yields ~58% of the available light with a total Teflon thickness of $152 \pm 10\,\mu$m. To provide electronic shielding, each crystal is wrapped in addition with $25\,\mu$m of aluminum foil.

A more efficient, automated approach employing Tyvek, a spunbonded olefin paper produced by DuPont, is under investigation. Tyvek has a high diffuse reflectivity similar to Teflon for the same thickness but is considerably more robust. A further advantage over Teflon is that Tyvek can be printed with a pattern of dots to selectively absorb light, thereby producing the required tuning pattern in an automated fashion. It is also possible to bond the $25\,\mu$m aluminum shielding foil directly to the Tyvek.

Coating CsI crystals with clear Teflon AF as a sealant to reduce the effects of humidity on the crystal surface is also being evaluated. Teflon AF has a low index of refraction compared to CsI and transmission measurements at the peak wavelength of scintillation emission (560 nm) indicate that the amount of light leaving the end of the crystal increases by about 5% compared to an uncoated crystal. A 2.54 cm-diameter by 2.54 cm-height CsI cylinder with diamond-polished end faces was coated with Teflon AF, and its transmission was measured. The crystal was then placed in a room-temperature chamber with 100%

humidity for three days. No change was observed in the transmission of the crystal after this exposure. The radiation hardness of Teflon coatings has been studied, and no change in optical properties for exposures of 40 krad of ^{60}Co γ-rays has been observed.

Water-based cross-linkable fluorocarbon (WXF) offers the same performance as Teflon AF but with a simpler dipping or brushing application and a lower temperature curing step. WXF can be applied in thicker coatings as well.

Both Teflon AF and WXF can be loaded with white TiO_2 powder to provide a highly reflective, diffuse coating. We are studying the application of a clear coating (to mimic a low index of refraction air layer) followed by a white diffuse coating (to mimic a wrapping of PTFE film, for example). This coating system offers greater control of thickness than is obtainable with wrappings.

Uniformity Specifications

The simulation results of Section 7.3.1 allow specification of light output uniformity. The nonuniformity contribution must be well below the target energy resolution (Equation 7.1). Requiring a contribution to σ_E/E below 0.5% translates into an integral variation of the light output between -6% and $+6\%$ from the front end to the back end of the crystal, as shown in Figure 7-22. Variations near shower maximum are the most critical. However, short distance variations of 2% in the front third of the crystals are tolerable (Figure 7-22). A procedure for measuring the light output uniformity is described in Section 7.4.3.

7.4.3 Light Yield Measurements

A number of crystals having dimensions similar to our baseline design were obtained from potential vendors and the light yields measured [Jes95a]. The readout techniques, shaping times, polishing, wrapping, and preparation are close to that of the baseline design.

The tests were made with a wrapping of three layers of PTFE Teflon film (each 38 μm thick) with one layer of aluminum foil outside. The light yield has been measured in three ways:

1. A 3.4 mm-thick WLS and two $30 \times 3.4\,\mathrm{mm}^2$ S3588-03 diodes was epoxied to adjacent edges. Two standard calorimeter preamps were used, with the WLS positioned 0.5 mm from the back face of the crystal.

2. Two $10 \times 20\,\mathrm{mm}^2$ S2744-03 diodes were directly coupled to the crystal using optical grease. Two standard calorimeter preamps were used.

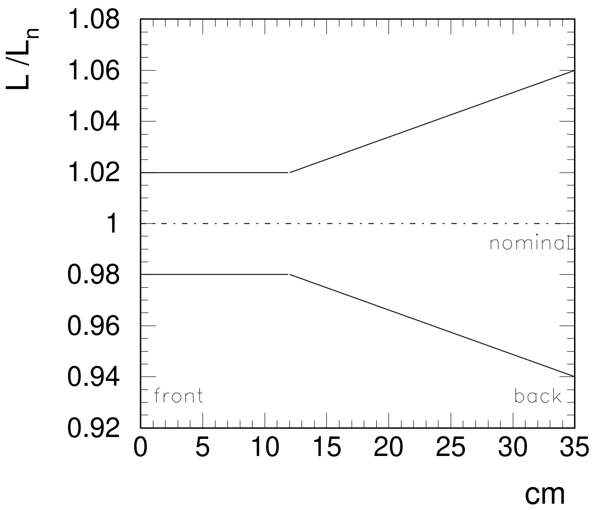

Figure 7-22. *Upper limits for the light output nonuniformity in a 35 cm-long CsI(Tl) crystal, assuming no more than 0.5% contribution to σ_E/E for all photon energies up to 5 GeV.*

3. A two-inch photomultiplier tube (Hamamatsu R669) with an extended-red multi-alkali photocathode (peak sensitivity at 650 nm) was positioned 0.5 mm from the crystal back face. The light yield is measured relative to that from a small calibration crystal, since this will be the procedure used for vendor specifications.

For the photodiode readout, the output signal is shaped using a $2\,\mu$s shaping time. Figure 7-20 shows how the relative light yield varies with shaping time. The absolute calibration of electron number per ADC channel for the diode is obtained by using a 59.5 keV x-ray from a ^{241}Am source, taking into account that 3.62 eV is required to produce one electron-hole pair in silicon.

Light Yield Specification

The light yield of CsI(Tl) crystals is directly related to the resolution and the energy-equivalent electronic noise. To ensure that the calorimeter can achieve the required performance, every crystal must satisfy a light yield specification supplied to the crystal manufacturers.

The light yield is sensitive to the thallium iodide concentration in the crystal, the light attenuation length, the shape and size of the crystal, the surface preparation, the wrapping, and the position of the source which introduces the scintillation. It is necessary to provide a practical and economical measurement procedure for the vendor. Therefore, the light yield

Vendor	Front Dim. (cm^2)	Rear Dim. (cm^2)	Length (cm)	LY Rel. to Std. (%)	LY Direct (*pe*/ MeV)	LY WLS (*pe*/ MeV)
Kharkov	25	25	34	32	6340	4200
Kharkov	34	20	34	32	5960	4600
Crismatec	28	18	23	27	4820	3650
Crismatec (hex)	28	18	22	31	5300	4250
Horiba	28	18	23	30	8600	5560
Horiba (hex)	28	18	23	50	9800	6800
Polsyscine	34	20	34	35	6500	4550

Table 7-8. *Light yield (LY) measurements (as described in the text) for full-sized crystals [Jes95a]. All crystals have a square cross section except where indicated.*

specification is given in terms of light yield relative to a small (*e.g.,* 2.54 cm diameter × 2.54 cm height) standard CsI(Tl) crystal, measured using γ lines from a radioactive source such as ^{22}Na, and a red-sensitive PMT. Light yield for a full-sized crystal can be defined as the average of a set of measurements taken at different source positions along the length of the crystal; such measurements are also used in determining the crystal's light output uniformity.

Assuming the WLS readout option, with 620 e^-s ENC for each crystal, a light yield of $620/0.15\,\mathrm{MeV} \approx 4100\,\mathrm{photoelectrons/MeV}$ is required to obtain 150 keV incoherent noise. From Table 7-8, a relative light yield of $\geq$ 30% is therefore required from each wrapped crystal.

7.4.4 Reliability of Inaccessible Readout Components

The barrel crystals and their front-end readout up to the ADC boards are inaccessible, barring disassembly of the detector. It is anticipated that this will not take place until ten years after the commissioning of the detector. Endcap crystals are relatively accessible and can be repaired on a much shorter time scale. We therefore require that no barrel crystal should fail in ten years. Achieving this reliability requires screening for defective parts before assembly and establishing an adequate natural lifetime for the remaining components.

The components most likely to fail are the connectors, bonds, and electronic components. Mechanical and thermal stresses and chemical aging may all be contributory factors. A stable thermal and humidity environment can reduce these effects.

A burn-in technique is being developed to screen all components, while random samples are collected to estimate the natural lifetimes by accelerated aging tests. Screening involves stressing components to remove those subject to infant mortality.

To establish the natural lifetime of components is difficult. It is empirically observed that, in the limit of a large number of components, each with a natural lifetime much greater than the operational lifetime, the failure rate follows an exponential distribution with a time constant 1/MTBF, the mean time between failures. This time is typically ≥ 100 years for electronics components, implying that a joint MTBF in excess of 60,000 years must be established if one requires less than one failure in 6000 crystals in 10 years. To establish this MTBF with certainty requires testing 6000 components for 10 years, which is not feasible. There are three techniques available to estimate the MTBF:

1. Assume aging is proportional to some power of temperature T^{α} (the Arhenius rate reaction formula). Test a number of components at high temperature and scale to the operating temperature. The power α can only be estimated from similar studies.

2. Use published formulae for estimating the failure rates of components based on experience from, *e.g.,* the military [Mil90].

3. Extrapolate failure rates from similar experiments such as CLEO-II, which operates 32,000 photodiodes and preamplifiers under similar conditions.

Adopting method (3), Table 7-9 lists cumulative diode and preamplifier failures and noisy diodes over five years of operation. The initial 48 diode failures are attributed to connector failures or insufficient screening. Considering all 48 plus the 14 noisy diodes as failures, the preamplifier appears far more likely to fail than the diode.

Using Poisson statistics, at the 95% confidence limit, one finds $\mathrm{MTBF}_{\mathrm{diode}} \geq 1954$ years, $\mathrm{MTBF}_{preamp} \geq 832$ years and combined, $\mathrm{MTBF}_{diode+preamp} > 643$ years. The WLS option uses diodes of similar area and manufacture, implying 93 failures per 6000 crystals after 10 years if a single diode/preamp readout is chosen. Table 7-10 shows the number of failing crystals as redundancy is increased, assuming $\mathrm{MTBF}_{diode+preamp} > 643$ years. Twofold redundancy yields 308 crystals with one dead channel and two crystals with two dead channels after 10 years [Jes95b]. A crystal with one dead channel has half the light yield and $1/\sqrt{2}$ the electronic noise in ENC, hence $\sqrt{2}$ higher equivalent noise energy.

Time (Months)	Diode Failures	Noisy Diodes	Preamplifier Failures
0	48	0	17
5	48	2	58
12	48	7	85
24	48	12	100
32	48	12	112
38	48	12	119
50	48	13	128
60	48	14	142

Table 7-9. *Cumulative diode and preamp failures for the CLEO-II calorimeter from 1989 to 1994.*

Failed Channels	1 Diode 1 Preamp	2 Diodes 2 Preamps	3 Diodes 3 Preamps	4 Diodes 4 Preamps
0	5907	5815	5725	5635
1	93	184	271	356
2		1	4	9
3			0	0
4				0

Table 7-10. *Number of failed channels on a crystal for various levels of redundancy, after 10 years, assuming the MTBF of (diode+preamp) is greater than 643 years.*

7.5 Calibration

7.5.1 Requirements and Ingredients

Several methods will be used in calibrating:

1. Electronics calibration will be done at least weekly with beams off. The ~2000 events needed per channel can be collected in several minutes. Calibration will entail the injection of charge at the preamplifier input, with controllable amplitude, phase (with respect to digitization), and pattern, using the system described in Chapter 10, in order to determine the detailed response function for each channel of electronics.

2. Bhabha events will be used for tracking overall gains. Enough data for this can be obtained on a timescale of well under a day.
3. Photons and electrons of known energy, as well as minimum ionizing tracks, will be used to set the energy scale (gain), including inter-channel variation of crystal light output and optical properties of the photodiode (WLS) readout.
4. Radioactive γ sources will provide low-energy point(s) for the response of individual crystals. Energy deposited in the front of a single crystal can be compared to Bhabhas in order to track optical changes. The source spectrum is a direct monitor of noise in energy units.

Items (2) and (4) also allow us to track changes over time of the entire optical path, including possible radiation damage or environmental changes. CLEO-II has achieved a calibration accuracy of $\pm0.2\%$ at $\sim$5 GeV increasing to $\pm1\%$ at 25 MeV, and a time-dependent gain stability of under $\pm0.25\%$ [Kub92]. *BaBar* can at least equal this performance and improve on the accuracy at low energies because lower electronic noise allows the use of radioactive sources. Although it is not part of the baseline design, a fiber optic distribution of light pulses is still under consideration for monitoring crystals.

The calibration system will be used to set initial gains for all channels to within $\sim$10%, to provide approximate real-time calibration factors for forming trigger sums and to provide online diagnostics.

7.5.2 Energy Calibration with Beam Events

At design luminosity, the total rate of Bhabha coincidences (above 300 mr) is $\sim$92 Hz, with at least 28 Bhabha $e^{\pm}$ per hour incident on each crystal. Since the mean fraction of energy in the peak crystal is $\sim$0.7, at least half of these events should be usable for calibration with either an iterative procedure or a fit. The goal of $\leq 0.25\%$ precision requires about 40 usable events in a crystal, which can be achieved in under three hours. For polar angles backwards of 133°, Bhabha singles must be used. A special trigger can prescale such events as a function of polar angle to obtain the sample.

The crystal response *vs.* energy must be mapped using photons of known or constrained energy. The process $e^+e^- \rightarrow \gamma\gamma$ provides maximum-energy data at each polar angle. In $e^+e^-\gamma$ and $\gamma\gamma\gamma$ final states, the energy of the lower energy photon can be computed from event topology. Radiative Bhabha yields have been calculated for a minimum separation of 15° between the photon and each lepton. At design luminosity, the usable yield of photons above 1 GeV ranges from 10 to 300 per hour per GeV per 10° of polar angle, varying across photon phase space. Lower energy photons can be obtained from $\pi^0 \rightarrow \gamma\gamma$ decays; on the order of one π^0 per $B\bar{B}$ event is expected to be usable. These are the methods by which CLEO-II presently covers the photon energy range of interest.

High-energy minimum ionizing tracks deposit most of their dE/dx loss, averaging $\sim$200 MeV, in individual crystals, providing a useful high-statistics comparison to Bhabhas. The yield from the $\mu^+\mu^-$ final state alone is at least 0.7 per hour per crystal, but non-interacting $\pi^\pm$ with momentum greater than 2.1 GeV/c, which traverse $\leq 2/3$ of a crystal in azimuth, will also be useful.

7.5.3 Source Calibration

Radioactive γ sources are included in the baseline design for several reasons. First, since the energy is deposited at the front of a crystal, comparison to Bhabhas will help identify the origin of a change in crystal gain, *e.g.,* radiation damage or other change in light collection. Second, a source spectrum provides a direct monitor of noise in energy units. Third, sources are the easiest way to make initial gain settings. Fourth, sources provide low-energy points for the responses of individual crystals to actual photons. Fifth, integrated sources do allow continual system checks after installation and whenever the accelerator is not running. Source energies of 2 MeV or higher are desirable to allow for cases of bad electronic noise and to better mimic photons of physics interest.

Source runs will be performed with beams off using a special processing mode which involves a search for signal waveforms in video RAM memory and the extraction of their amplitudes. A source activity of 0.01 μC for one crystal implies 1000 usable events in ten seconds. An actual source run will be longer, due to processing limitations, but still well under 20 minutes.

Three options are under study:

1. Mounting 0.01 μC ^{60}Co sources ($t_{1/2} \approx 5$ years) at the front face of each crystal and using the 2.51 MeV sum line. For adequate efficiency, this may entail inserting a source at the end of a fine needle into a very narrow hole drilled several centimeters into the front of the crystal. The feasibility of this approach is being evaluated.

2. Pneumatically inserting several 100 μC sources at $z = 0$ just outside the support tube or within the PID enclosure. A good candidate is ^{208}Tl, which has a 2.614 MeV γ line, driven by an α decay chain from ^{228}Th ($t_{1/2} \sim 2$ years) or ^{232}U ($t_{1/2} \sim 100$ years). Encapsulation prevents α particles or radon from escaping.

3. Circulating about 1000 cm^3 of liquid, activated in a shielded neutron source located outside the detector, through fine tubes running in front of all crystals. Choices include: (a) A fluorine-containing fluid, with a metastable state of ^{16}O via ^{19}F (n,α) ^{16}N;

	Barrel (cm)	Forward Endcap (cm)
Inner Gas Seal	0.5	3.0
Crystal Box Extension	0.1	0.7
Inward Dimension Tol.	0.6	0.6
Crystal Length	29.76–32.55	32.55
Outward Dimension Tol.	0.6	0.6
WLS/Diode Package+Spacers	0.4	0.4
Gap to Preamplifier	0.1	0.1
Preamplifier/Header	2.6	2.6
Cooling Manifold	1.5	1.2
Module Insertion Fixture/Cables	2.5	
Module Strongback	1.6	
Alignment Jacks	2.5	0.8
Aluminum Strongback /Frame	3.2	2.0
Total	46.0	44.5

Table 7-11. *Thickness of the calorimeter assembly, barrel, and endcap.*

neutrons of ~4-6 MeV from a Po-Be source are appropriate. The decay provides a 6.13 MeV γ line, with $t_{1/2}$ of only 7 sec. This choice has been assessed as posing no significant radiation safety hazard. (b) Water, with ^{16}O (n,p) ^{16}N leading to the same γ line. Activation could be by 14 MeV neutrons from a DT source. By using saltwater and a moderated neutron source, one could additionally provide 2.75 MeV and 1.37 MeV γ lines (with $t_{1/2}$ of 15 hours) via ^{23}Na (n,γ) ^{24}Na.

7.6 Mechanical Support Structure

7.6.1 Design Considerations

The mechanical structure of the *BaBar* calorimeter is designed to minimize inactive material between individual crystals, while providing hermeticity at the barrel-endcap interface. Access, testing, repair, and reliability are addressed in the design of the overall structure, as are the crystal loading procedures, and installation and system integration. RF shielding and cooling of electronics, cable routing, and humidity control considerations are also discussed in the following sections. Table 7-11 details the radial dimensions of the barrel and forward endcap.

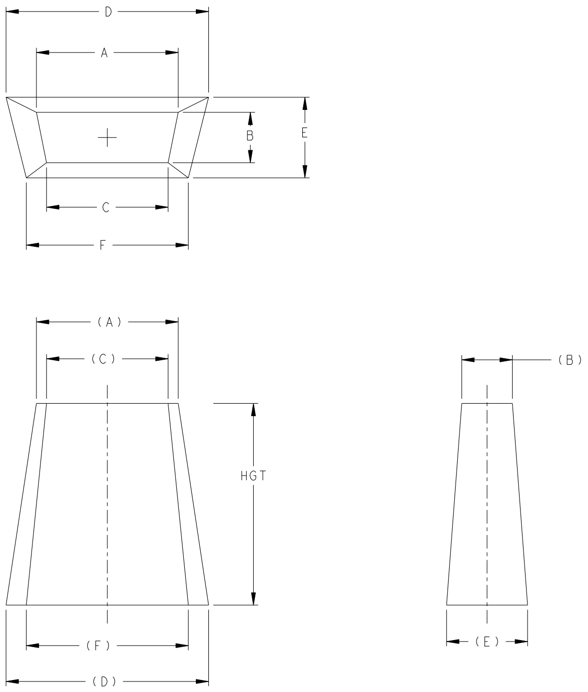

Figure 7-23. *Crystal dimensions (Tables 7-12 and 7-13).*

Since the detector is located in a seismically active region, safety standards require that the calorimeter be designed to withstand accelerations of up to 2 g horizontally and 1 g vertically, without significant damage, both during the assembly period and after installation.

Crystal Loading, Sizes, and Tolerances. CsI(Tl) is grown in polycrystalline form and is a soft, deformable material that cannot support substantial loads. Therefore, the structure must support individual crystals without transferring the load through neighboring crystals.

The crystal sizes and counts for the barrel and endcap are given in Tables 7-12 and 7-13. The columns in the tables give the dimensions of the crystal edges as shown in Figure 7-23.

Crystals are required to fit loosely into their barrel or endcap compartments. Crystal dimensional tolerances are summarized in Figure 7-24. The tolerance on crystal transverse dimensions ($\pm 225\,\mu$m) allows the cost of cutting and polishing to be minimized. Consequently, an additional radial space of 0.5 cm is required, as indicated in Table 7-11.

Wall Material and Thickness, and Inter-Crystal Material. Properties of structural materials under consideration for the compartment walls are given in Table 7-14.

θ Row	Number Needed	Volume (cc)	A (cm)	B (cm)	C (cm)	D (cm)	E (cm)	F (cm)	Height (cm)
1	120	882.5	4.956	4.773	4.736	5.779	5.523	5.524	32.55
2	120	888.4	4.953	4.773	4.736	5.812	5.559	5.559	32.55
3	120	894.6	4.950	4.773	4.736	5.846	5.595	5.594	32.55
4	120	901.0	4.947	4.773	4.736	5.880	5.633	5.631	32.55
5	120	907.6	4.943	4.773	4.736	5.916	5.672	5.669	32.55
6	120	914.4	4.939	4.773	4.736	5.952	5.712	5.708	32.55
7	120	921.3	4.935	4.773	4.736	5.988	5.753	5.748	32.55
8	120	896.7	4.930	4.773	4.736	5.994	5.766	5.759	31.62
9	120	903.5	4.925	4.773	4.736	6.030	5.808	5.800	31.62
10	120	910.4	4.919	4.773	4.736	6.065	5.850	5.841	31.62
11	120	917.3	4.913	4.773	4.736	6.101	5.893	5.882	31.62
12	120	924.4	4.907	4.773	4.736	6.136	5.936	5.924	31.62
13	120	931.4	4.900	4.773	4.736	6.171	5.980	5.965	31.62
14	120	938.3	4.892	4.773	4.736	6.204	6.023	6.007	31.62
15	120	910.6	4.884	4.773	4.736	6.197	6.028	6.009	30.69
16	120	916.9	4.876	4.773	4.736	6.226	6.069	6.048	30.69
17	120	922.9	4.867	4.773	4.736	6.254	6.108	6.086	30.69
18	120	928.7	4.857	4.773	4.736	6.279	6.147	6.123	30.69
19	120	934.2	4.847	4.773	4.736	6.302	6.184	6.158	30.69
20	120	939.3	4.837	4.773	4.736	6.322	6.220	6.191	30.69
21	120	943.9	4.826	4.773	4.736	6.339	6.253	6.222	30.69
22	120	911.3	4.814	4.773	4.736	6.306	6.237	6.204	29.76
23	120	914.6	4.802	4.773	4.736	6.315	6.264	6.228	29.76
24	120	917.2	4.790	4.773	4.736	6.320	6.287	6.248	29.76
25	120	919.2	4.778	4.773	4.736	6.321	6.307	6.266	29.76
26	120	920.6	4.765	4.773	4.736	6.318	6.322	6.279	29.76
27	120	921.2	4.752	4.773	4.736	6.310	6.334	6.289	29.76
28	120	882.4	4.740	4.773	4.736	6.299	5.896	6.294	29.76
29	120	882.4	4.740	4.773	4.736	6.299	5.896	6.294	29.76
30	120	921.2	4.752	4.773	4.736	6.310	6.334	6.289	29.76
31	120	920.6	4.765	4.773	4.736	6.318	6.322	6.279	29.76
32	120	919.2	4.778	4.773	4.736	6.321	6.307	6.266	29.76
33	120	917.2	4.790	4.773	4.736	6.320	6.287	6.248	29.76
34	120	914.6	4.802	4.773	4.736	6.315	6.264	6.228	29.76
35	120	911.3	4.814	4.773	4.736	6.306	6.237	6.204	29.76
36	120	907.5	4.826	4.773	4.736	6.293	6.208	6.177	29.76
37	120	903.2	4.837	4.773	4.736	6.277	6.176	6.147	29.76
38	120	898.4	4.847	4.773	4.736	6.258	6.142	6.115	29.76
39	120	893.4	4.857	4.773	4.736	6.236	6.106	6.081	29.76
40	120	888.0	4.867	4.773	4.736	6.212	6.068	6.045	29.76
41	120	882.3	4.876	4.773	4.736	6.185	6.029	6.008	29.76
42	120	876.5	4.884	4.773	4.736	6.157	5.990	5.971	29.76
43	120	870.5	4.892	4.773	4.736	6.127	5.949	5.932	29.76
44	120	864.4	4.900	4.773	4.736	6.096	5.909	5.893	29.76
45	120	858.3	4.907	4.773	4.736	6.064	5.868	5.854	29.76
46	120	852.2	4.913	4.773	4.736	6.031	5.827	5.815	29.76
47	120	846.1	4.919	4.773	4.736	5.998	5.787	5.776	29.76
48	120	840.0	4.925	4.773	4.736	5.965	5.747	5.737	29.76
49	120	834.1	4.930	4.773	4.736	5.931	5.708	5.699	29.76

Table 7-12. *Crystal dimensions and counts for the barrel. Dimensions A through F are defined in Figure 7-23.*

θ Row	Number Needed	Volume (cc)	A (cm)	B (cm)	C (cm)	D (cm)	E (cm)	F (cm)	Height (cm)
1	80	741.0	4.298	4.670	3.944	4.995	5.426	4.583	32.55
2	80	802.4	4.641	4.670	4.289	5.394	5.428	4.985	32.55
3	80	863.6	4.982	4.670	4.632	5.792	5.430	5.386	32.55
4	100	739.6	4.247	4.670	3.970	4.941	5.432	4.618	32.55
5	100	788.3	4.519	4.670	4.244	5.257	5.433	4.937	32.55
6	100	836.9	4.790	4.670	4.517	5.573	5.433	5.256	32.55
7	120	737.7	4.209	4.670	3.984	4.898	5.434	4.636	32.55
8	120	778.4	4.437	4.670	4.214	5.162	5.433	4.903	32.55
9	120	819.1	4.665	4.670	4.445	5.427	5.432	5.171	32.55

Table 7-13. *Crystal dimensions and counts for the endcap. Dimensions A through F are defined in Figure 7-23.*

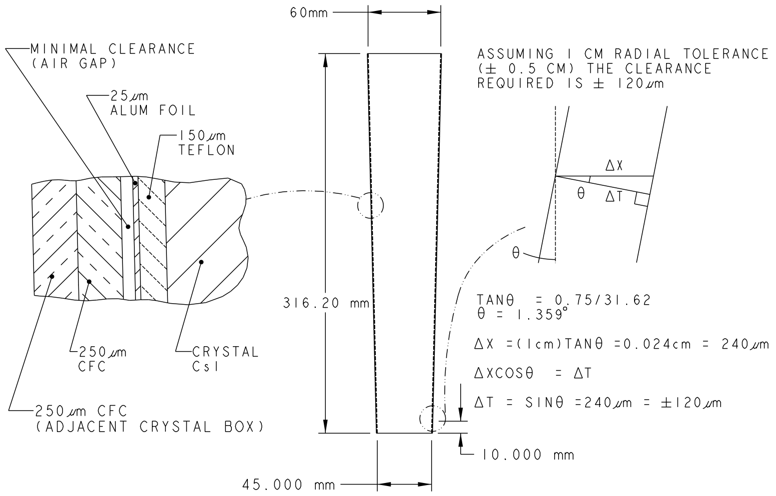

Figure 7-24. *Crystal and wrapping tolerances.*

Wall Materials	Density (g/cm^3)	dE/dx (MeV/g/cm^2)	X_0 (g/cm^2)
Carbon Fiber	1.68	1.90	45.2
Glass Fiber	1.70	1.87	33.0
Aluminum	2.70	1.62	24.0

Table 7-14. *Structural-material properties (assumes 40% epoxy and 60% fiber loading for fiber materials).*

CFC with 250 μm wall thickness has been chosen for crystal compartments because it has the best combination of strength and minimum material (X_0). There are two such walls between crystals, resulting in a total amount of structural material between crystals of $2 \times 0.09\%$ X_0. Mechanical tolerances of the CFC boxes that form the support structure can be made small because the boxes are formed on accurate mandrels and assembled in precision trough fixtures. (The fabrication technique in the endcap places a different set of requirements on the dimensions.)

Inactive material between crystals also includes reflective wrappings, shielding foils, and airgaps due to mechanical tolerances. This adds another $2 \times 0.07\%$ X_0, resulting in a total of $2 \times 0.16\%$ X_0 between crystals.

Nonprojectivity. To minimize unmeasured energy due to inactive material between crystals, the crystals are arranged to be slightly nonprojective in θ and projective in ϕ with respect to the IP. The degree of nonprojectivity is set by the requirement that straight-line tracks cannot be completely contained in the gaps between individual crystals. Simulations show that degradation of reconstruction efficiency begins for photons that traverse more than one fourth of the gap length before entering a crystal. To prevent this degradation, a fixed θ offset of 15 mr is added to the projective angle for a given crystal and this offset is applied to each crystal in the barrel and endcap. The crystals then project to a point that varies between 2 mm and 5 cm from the IP along the beam line. To minimize the number of unique crystal shapes, the crystal gap is centered projectively at $90°$ with respect to the beam line. The front faces of the crystals are uniform in width and perpendicular to the crystal axis. In ϕ, the crystals are arranged so that the center lines of their compartment gaps project to the beam axis.

The crystal row of the last barrel and first endcap at the forward barrel/endcap interface require special treatment because of the larger gap in this region. They will be shaped so that the barrel/endcap gap is sufficiently nonprojective.

RF Shielding of the Electronics. The barrel and endcap are constructed as separate Faraday cages. The inner rf-shields are provided by a laminate of two layers of 1 mm-thick aluminum (each about four skin-depths at 100 kHz) separated by a thin foam core. The interface region between the inner and outer faces of the barrel and forward endcap are tied together with flexible metallic fingers to shield the 3 mm gap. Shielding for inter-crystal cross-talk and rf noise from the preamplifiers and photodiodes of an individual crystal is provided by aluminum enclosures attached to the 25 μm aluminum wrap of the crystal.

Environmental Control for Crystals and Electronics. The calorimeter will be kept at an appropriate constant temperature in order to keep the leakage current of the photodiodes below 2 nA, to maintain stable preamplifier performance, and to keep a constant CsI(Tl) scintillation light yield.

The two preamplifiers for each crystal generate about 100–250 mW, giving a total heat load inside the rf-shield of about 2.5 kW. Heat flow calculations on a model crystal assembly with the conservative assumption of 500 mW total power generated at the electronics indicate that active cooling is required. Thermal control to better than $\pm 1°$C is achieved by flowing coolant into the calorimeter along circumferential manifolds into pipes running axially along the crystal rows. Each crystal's electronic shield is attached by braid to the manifold. The cooling system output is cycled through an external heat exchanger. Digitizing electronics located in shielded enclosures at the end of the barrel calorimeter housing and the outer rear of the endcap are cooled using the same system.

The outer surfaces of the calorimeter form a gas enclosure for humidity control. Dry nitrogen flowing through the volume at a slow rate and slight overpressure is used to maintain a dry atmosphere to prevent degradation of the crystal surfaces.

Signal and Control Routing. Signal and control cables are passed through the Faraday/environmental shield using sealed bulkheads containing signal feedthroughs. Signal cable lengths between preamplifiers and bulkheads are minimized, with the longest run being approximately 1.5 m. A standard 12-pair shielded cable will be used.

Digitizing electronics cards are attached to the feedthrough connectors in the bulkheads. Fiber-optic cabling from the digitizer cards of both the barrel and forward endcap is routed outward between the barrel and endcap flux return iron.

Access and Component Replacement. Individual barrel crystals and their readout packages are not accessible once the calorimeter has been installed in the solenoid. However, the modular design facilitates testing and replacement of diode/preamp packages before this installation. The endcap can be removed for internal maintenance. All calorimeter digitizer cards can be readily accessed for repair by opening the endcap doors.

7.6.2 Barrel Fabrication, Assembly, and Installation

Barrel System

In order to avoid the transmission of loads through the crystals, the barrel cylinder is divided into independently supported and aligned modules which have little or no mechanical contact with each other. Their light weight limits deflections. The structure is composed of CFC elements between crystals in which minimum material is necessary, and aluminum plates in which structural strength is required and more material can be tolerated.

The basic units are the CFC compartments (boxes) that house individual crystals. The CFC boxes are combined into modules containing 3×7 crystals, each weighing approximately 80 kg. Figure 7-27 shows the basic module structure. The individual compartments are stiffened at their rear (outer) ends with a ring that also corrects for tolerances in the crystal placement and locks the crystal longitudinally into position in their boxes. The boxes are joined to a strongback made from thin aluminum side plates (tabs) and an extruded aluminum U-channel fastened to the rear of the modules. The module strongbacks transmit loads to a large cylindrical aluminum tube with stiffening flanges at each end, into which the modules are inserted and aligned. Both the module strongback and the cylindrical tube have access ports to allow for assembly, alignment, cabling, and repair prior to insertion into

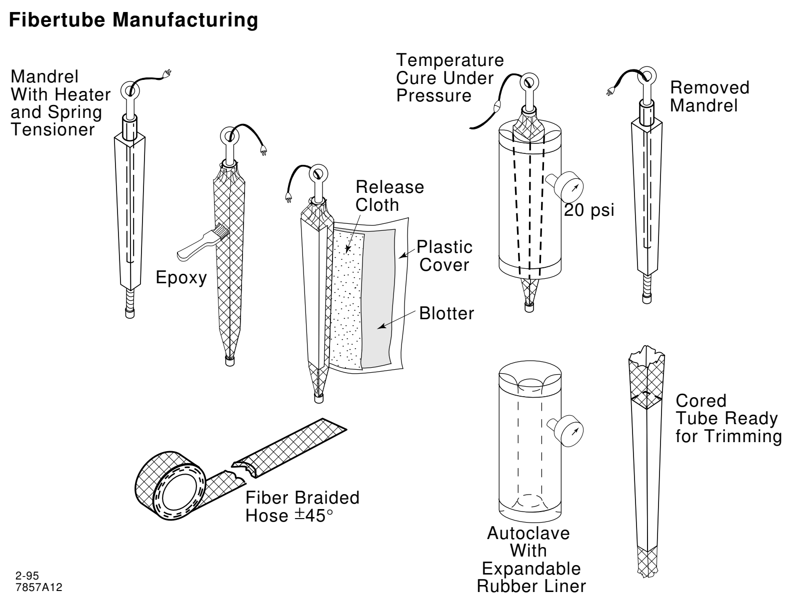

Figure 7-25. *Schematic of tube fabrication by a wet-layup technique.*

the magnet coil. After insertion into the coil, the tube transmits its load to the coil and flux return through a two-point mounting scheme on each end flange.

Module Fabrication

The choice of module size is made by considering ease of handling (without requiring large cranes or special fixtures within dry-rooms), access to elements within, size and complexity of fabrication fixtures, and the deflections and strengths of the elements. The delivery schedule of each crystal type, and its influence on the assembly schedule, is also considered. There are 280 modules in the barrel, 40 in azimuth and 7 along the beam axis.

Each CFC box is fabricated using a conventional wet (epoxy-resin) layup technique, as illustrated in Figure 7-25. This technique allows reproducible dimensions of the inside box. The final wall thickness is the only variable dimension. For each crystal size, an aluminum master mandrel is precision machined to the size of a wrapped crystal (*i.e.,* crystal dimension plus $\sim 175\,\mu$m). The mandrel contains a heating and thermostatic control element for curing the epoxy. The mandrel blanks may be fabricated by casting.

To fabricate a CFC box, the mandrel is first sprayed with a release agent such as Teflon. A woven tube, or sock, of CFC is stretched over the mandrel. The weave is chosen at ± 45–$60°$ to accommodate the taper of the crystal. Socks will be custom fabricated to a finished thickness of 250 μm. These contain 400 strands per inch of 25 μm filament. The mandrel will be covered with a 25 μm aluminum foil electronic shield before placing the sock over the mandrel. The sock is next uniformly impregnated with thermal-setting epoxy resin. The mandrel and sock are wrapped together in peel-ply, bleeder cloth, and a protective polyvinyl sheet. The layup is cured under 2 atm pressure applied uniformly by a simple fixture at 40°C using a heater in the mandrel. After the ~2 hour cure, the tube is removed from the mandrel and trimmed to shape and length. The mandrel and tooling are reused. Tests performed over the last three years (Figure 7-28) using CFC boxes of similar weave fabricated with this technique and with several commercial epoxy systems indicate that the dimensional creep of such boxes is acceptable. Small factories can be set up at various collaborating institutions to fabricate the 5880 elements for the calorimeter barrel.

There are seven distinct module types along the length of the barrel, for which 40 modules in ϕ (plus one or two spares each) are required. The boxes are joined into 3×7 arrays for each of these module types by constructing an aluminum trough fixture with inside dimensions corresponding to the finished outside dimensions (symmetric wedge in ϕ and a three-faceted wedge on each θ end (Figure 7-27) of the desired unit. The trough fixture has stops along each of the 21 crystal axes (Figure 7-26) to set the depth. To lay up a module, a mandrel is inserted into each of the 21 boxes. The exterior surfaces of the boxes are roughened and wetted with epoxy. The tubes and mandrels are then forced into the trough, in rows of three, until all 21 spaces are occupied. By seating the ends at the depth stops, the epoxy is forced out automatically, accommodating the irregular shapes of the outer walls of the boxes while preserving the inside dimensions. The mandrel heaters cure the unit. Once cured, the mandrels are removed, leaving the module in the trough. Any excess epoxy is cleaned off, and the perimeter edges of the two outer rows of boxes are trimmed to their final shape.

The next module manufacturing step is the stiffening of the boxes and attachment of aluminum support elements at the rear of the box array. The trough and unfinished module are moved to a dry-room area so that each compartment can be loaded with its wrapped CsI crystal. An example of a suitable facility is Building 109 at SLAC, which contains an existing, high-quality 2–3% humidity dry-room. This room will be enlarged and refurbished with a high performance lithium-chloride-based dehumidifier to allow crystal and module storage, assembly, and electronic testing in the same area. The original dehumidifier for the building will be refurbished and used for the adjacent temporary assembly area, and as an emergency backup system.

To complete a module, each crystal is pushed forward into its compartment. The taper of the crystal module and the fabrication tolerance ensure that the crystals will sit loosely within the box (± 0.5 cm from nominal radial position). An aluminum enclosure (Figure 7-29) is inserted into the top and glued to the inside of the box with a small amount of conducting epoxy so that the crystal's foil wrap remains in good electrical contact with the enclosure. When all crystals are in place, the 1.27 cm-thick rear extruded aluminum U-channel strongback

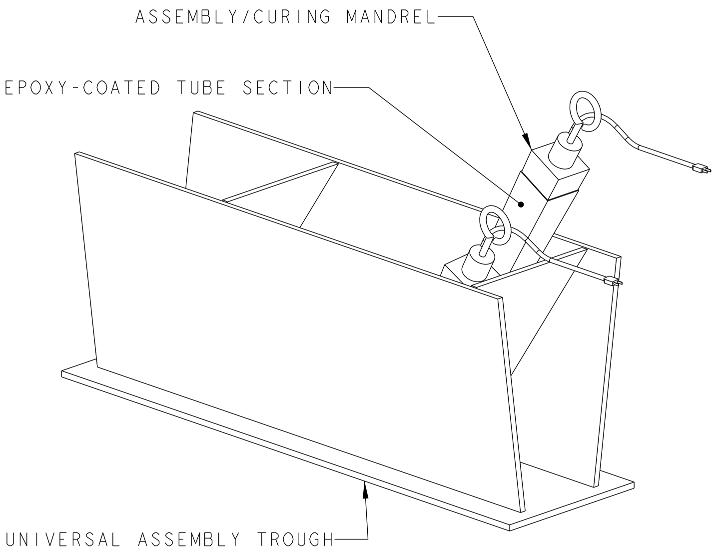

Figure 7-26. *Trough fixture for combining tubes into module subassemblies.*

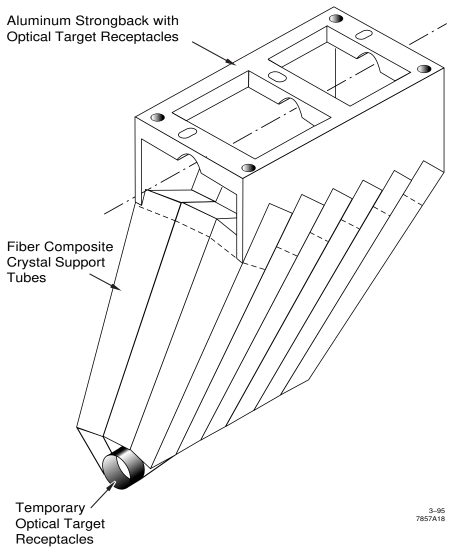

Figure 7-27. *Schematic of a barrel module.*

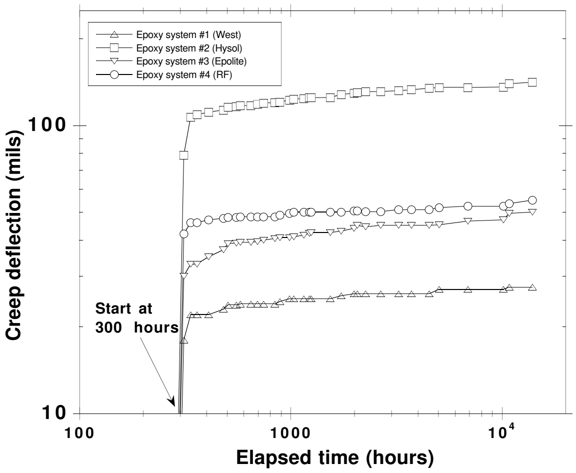

Figure 7-28. *Creep tests of glass-fiber woven boxes prepared by a wet-layup technique.*

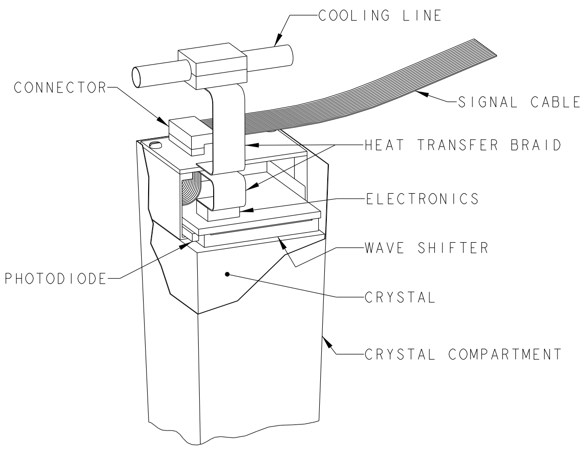

Figure 7-29. *Detailed side view of a module showing crystal, shielded readout package, cooling, and cabling.*

assembly is screwed and bonded to the side supports. Bridging elements are bonded in place to stiffen the module.

A set of wire alignment target holders are epoxied to each module as shown in Figure 7-27. Their position is set by the trough, allowing exact and reproducible placement of the targets.

Module Completion and Testing

When the module is completed and removed from its trough, it is placed into dry-room storage until electronics installation. The electronics assembly involves the addition of a wavelength shifter/diode package and preamplifier board to each compartment in a module. These elements attach to the aluminum enclosure and are spring loaded to press against the back face of the crystal. A lip machined into the aluminum enclosure maintains a uniform air gap between the WLS and the crystal. If the direct diode readout method is selected, crystals have their PIN diodes pre-attached (and pre-tested) before being inserted into the module. The preamplifier is connected by soldering the diode leads through plated vias in the preamplifier board, and the preamplifier card is strain-relieved to the enclosure cover. The stamped cover of 1.5 mm thickness is screwed down to the aluminum enclosure, making contact all around the perimeter. Cables enter through the top by means of a ribbon connector. The finished module may be tested and returned to dry storage prior to insertion onto the strongback cylinder.

Barrel Assembly

The assembly of the entire barrel and endcap calorimeter takes place adjacent to the dry-room in SLAC Building 109. A temporary dry-room ($5 \times 5 \times 5$ m) is constructed with unistrut, wire mesh, and inner and outer plastic sheet walls. Walls are sealed to an epoxy-painted concrete floor and dry air blown between them. This temporary assembly area is connected to the storage/testing dry-room by a short interlocked passageway through which modules can be carried from storage.

The assembly fixture is shown in Figure 7-30. The large cylindrical strongback is first mounted to a support frame at the two points on each of the end-flanges that will eventually be used for support by the coil. By mounting it in this way, the strongback can be transferred to the coil supports without affecting the alignment of the modules. Alignment of individual modules compensates for strongback and module distortions that occur during the loading procedure.

A module is moved to the assembly area after electronics testing. The strongback of each module is mounted vertically on a movable module insertion arm on an assembly fixture (Figure 7-30). The arm is rotated to the proper ϕ orientation and moved axially into

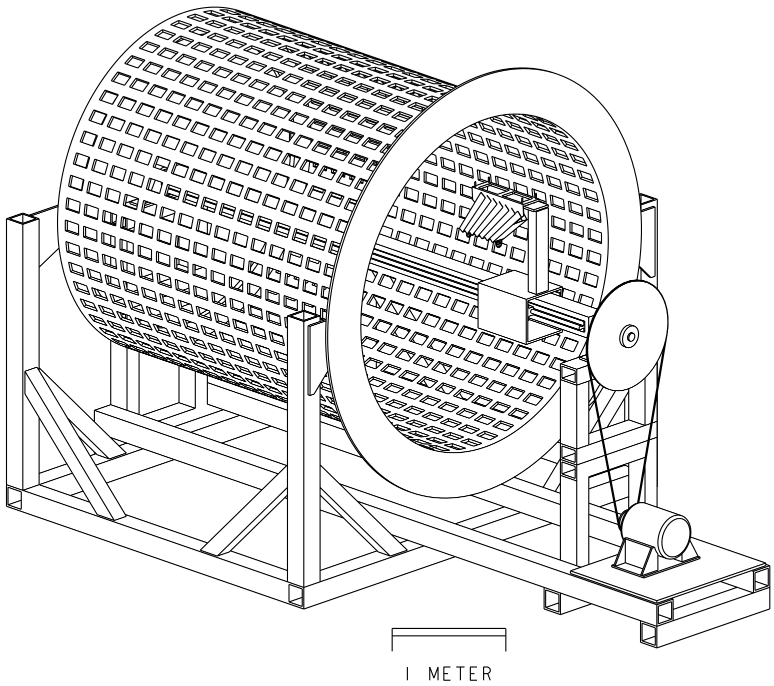

Figure 7-30. *Barrel assembly fixture for inserting and mounting modules in the strongback.*

place within the barrel. The module is then rough-mounted to the strongback. Initially, all modules are retracted radially about 2.5 cm from nominal, allowing space for adjacent modules to be installed. When all modules are loaded, the strongback cylinder will be in its fully deformed state. The alignment mechanism is then used to align each module into the correct radius and orientation.

The alignment procedure is accomplished by placing an accurately machined template on the ends of the strongback cylinder and iteratively aligning the pre-mounted wire alignment targets with the template in each of the 40 ϕ module rows. Alignment telescopes are mounted on the module installation arm for simplicity. The procedure is shown schematically in Figure 7-31. Two or more crews can work simultaneously to align separate rows of modules, and the alignment procedure itself does not add significant deformations to previously aligned modules. Thus, a single alignment pass should be sufficient.

Finite Element Analysis

A preliminary finite element analysis has been performed both on the strongback cylinder loaded with dummy modules and on a few representative individual modules. This approach

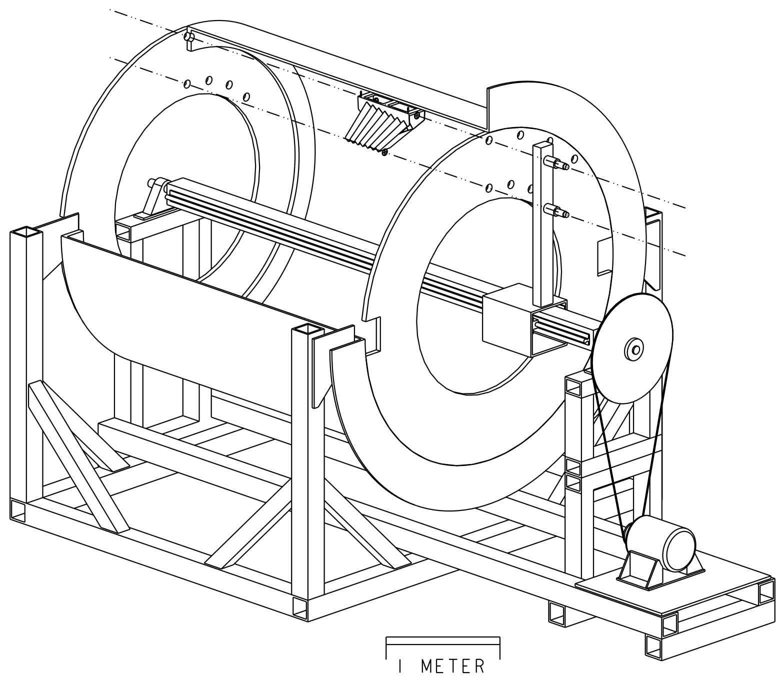

Figure 7-31. *Barrel alignment.*

is suggested by the independent suspension of the modules in the cylinder, allowing separate calculation of module deflections. The cylinder analysis determines an appropriate cylinder thickness, taking into account the amount of material removed for module access ports, and the required sizes of the forward and backward flanges. The forward(backward) end flange used in the cylinder analysis is 2.5 cm(5.0 cm)-thick and 36 cm(20 cm)-wide.

The strengthening tab thickness used in the model of a module is 0.64 cm. The analysis assumes for simplicity that the crystal boxes are made of 250 μm-thick aluminum sheets (the modulus of elasticity of aluminum is about the same as the quasi-isotropic modulus of CFC). While we will not have enough layers of carbon fiber to make the composite behave isotropically, the steep pitch of the sock fibers makes the box stiffer than aluminum in the bending-strain direction. The loading of the crystal boxes is assumed to be concentrated where the box walls meet at right angles because the box material is so thin that it will have little mid-span bending stiffness. Under these conditions, the loading shifts to these corners where the boxes are stiffest.

The module model includes a matrix of 1.0 mm-thick aluminum electronics enclosures assembled behind the crystals. These enclosures also serve to keep each thin CFC crystal box square at this end. Additional stiffeners are included in modules near the end of the cylinder, where the center of gravity of the crystals is farther from the cylinder wall. Stiffer support

Element	Deflection (mm)
Module in Horizontal (end)	0.40
Module in Horizontal (center)	0.42
Module in Vertical	0.04
Strongback Cylinder (unloaded)	0.04
Strongback Cylinder (loaded)	0.67
End Flanges (cylinder loaded)	0.04

Table 7-15. *Static deflections encountered in the barrel.*

is required in this region, but there is also more room for material without obstructing electronics and cable ways.

Static deflections of the system are summarized in Table 7-15. For example, when all modules are installed, the 3.175 cm-thick strongback cylinder is deformed by ~670 μm at the center of the cylinder. The inner faces of modules mounted in the horizontal plane undergo the maximum deflection expected, about 420 μm relative to the cylinder, or 1.1 mm total vertical deflection relative to the cylinder end flange mounting points. However, this 1.1 mm deflection is effectively removed during the final alignment of the crystal modules.

Testing and Closure: Cabling, Cooling, Front and Back Panels

When modules are first installed in the strongback cylinder, an *in situ* electronic test is performed to ensure that there are no problems with individual crystals that require removal and replacement of a module. Once the final alignment is done, the cooling manifolds and cooling tubes to each box are installed, followed by the final cable runs. Plumbing for dry-nitrogen gas circulation is installed as is the inner rf/environmental cylinder. In order to keep all plumbing electrically isolated from the cylinder, nonmetallic couplers are used on the outer connections to manifolds.

A sufficiently long system test is then performed to find any remaining problems in the electronics. Next, the strongback cylinder access ports are closed with sufficiently thick sheet metal to complete the Faraday cage and gas seal.

Barrel Installation into the Coil. The fully aligned, cabled, and tested assembly is carried to the assembly area for the coil and flux return in the detector hall. A system test is once again performed to check that no damage occurred during transport to the hall. Installation into the detector is discussed in Chapter 14.

7.6.3 Endcap Fabrication, Assembly, and Installation

Endcap Overview

The design of the endcap is quite different conceptually from that of the barrel. Once installed, the barrel will remain unopened, possibly for the lifetime or the experiment, whereas the endcap must be capable of rapid mounting and demounting while maintaining precision mating to the barrel. The mechanical structure is sophisticated, involving a high precision, rigid outer shell with minimal material between the crystals.

The forward endcap is a conic section, with front and back surfaces tilted at 22.7° to the vertical to match the drift chamber endplate, and is built in two monolithic pieces to enable rapid demounting for access to inner parts of the detector. It is supported off the solenoid coil and precisely aligned with the calorimeter barrel, and has been designed to minimize both the material and the air gap between the two. The geometry is almost projective, with the crystal axes pointing to an axial position 5 cm from the interaction point. The total weight of the endcap is approximately 4 tonne.

In order to preserve optimum light collection and both spatial and energy resolution, similar-sized crystals have been used throughout. This results in a layout of nine rings of trapezoidal crystals, grouped in three super-rings of 120, 100 and 80 crystals. The total number of crystals is 900, arranged in 20-fold symmetry.

Crystal Honeycomb Container

Each crystal package, consisting of crystal, readout electronics and cooling circuit, is held rigidly in a separate compartment of the honeycomb structure, which is glued inside a load-bearing container, as shown in Figure 7-32. Structural rigidity is obtained from the solid aluminum inner wall of the conic section, reinforced at the rear with a semicircular flange. Bonded to this inner wall is the front face of the box, formed from two aluminum skins of 1 mm thickness separated by a nomex core to give additional rigidity. These last two surfaces also form part of the Faraday cage enclosing the barrel and endcap. The faces of the container that mate to each other or to the barrel are made from 1 mm carbon fiber composite (CFC) and serve mainly to bond the honeycomb structure of crystal boxes. A semicircular flange is bonded onto the rear of the thin outer wall of the conic section, both to maintain its shape and form part of the structural support.

The honeycomb compartments are individually made in the form of tapered boxes of CFC of wall thickness 250 μm. The technique involves stretching a CFC sock over a mandrel, coating it with epoxy, and curing it under pressure. The honeycomb is built up from 20 identical, wedge-shaped modules, each consisting of 45 boxes. Assembly takes place in a precisiondimensioned aluminum trough. Mandrels are inserted into the boxes, the outer surfaces of which were previously roughened and coated with epoxy, and the whole cured under pressure. Ten modules are epoxied into each segment of the endcap, using a combination of mandrels and simple fixtures to ensure bonding to the walls of the container.

Structural Assembly

Each of the two containers is prepared for transport, or assembly, by installing radial rails, fitted with cooling circuits and pre-cabled trays, between the inner and outer semicircular flanges, and clamping the walls of each crystal compartment in the outer super-ring to a rail and tensioning them. The rails form a hub at the center, giving the necessary rigidity to circumferential shearing.

During crystal loading, the container is held vertically in an assembly jig which supports it from the front by means of the two rear flanges and the solid aluminum inner wall, shown in Figure 7-33. As each radial rail is removed in turn, crystal packages are loosely fitted into the compartments to rest on pre-measured styrofoam pads and secured with a square ring. The readout and preamplifier electronics unit for each crystal, pre-mounted with its heatsink on a cap, is screwed to the ring.

Heat sinks, electrical shielding and connections are secured to the rail and the outer crystal compartments clamped and tensioned. A final electrical test is performed on each group of crystals installed. The half ring support structure, with pre-mounted electrically shielded ADC housings (Figure 7-34), is bolted onto the outer flange of the container, and electrical connections made. The aluminum support plate is now bolted onto the support structure at its outer radius and the hub formed by the rails at its inner radius, and cover plates bolted over the access holes to complete the Faraday cage. Two assembly frames are required in order that each segment of the endcap may be completely prepared for installation.

Prototype Analysis

Stress analysis has been performed for individual crystal compartments, a module of 45 such compartments, and one segment of the endcap comprising a honeycomb of ten modules, using finite-element modelling of the loaded structures. The results indicate a rather uniform pattern of stresses and deformations with maximum values of 10 MPa and 0.1 mm respectively.

Because of the precision required in mating the barrel and endcap, it may be necessary to build a mechanical pre-production prototype consisting of a half-endcap, install it in the assembly frame and load it with weighted blocks having similar properties to CsI. Measurements taken with strain gauges might then be compared with predictions from the

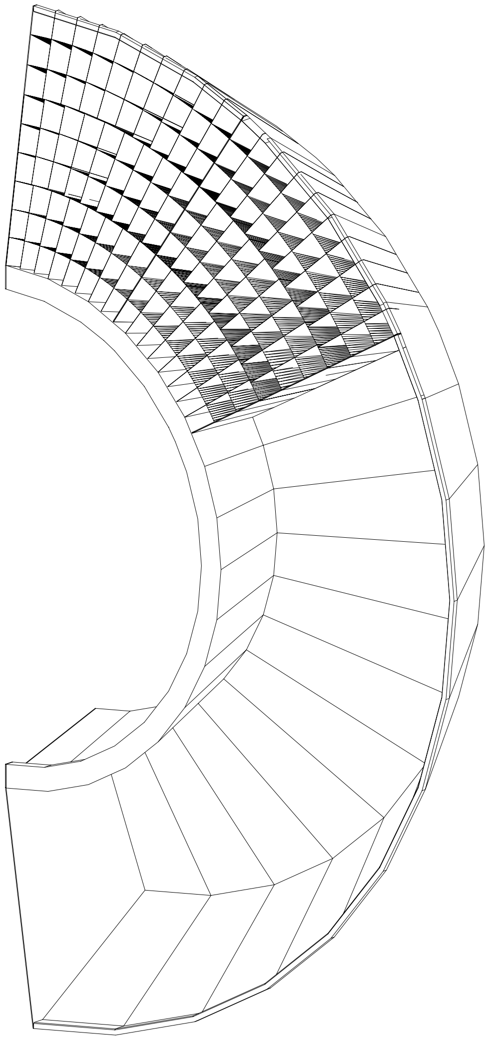

Figure 7-32. *Endcap load-bearing container.*

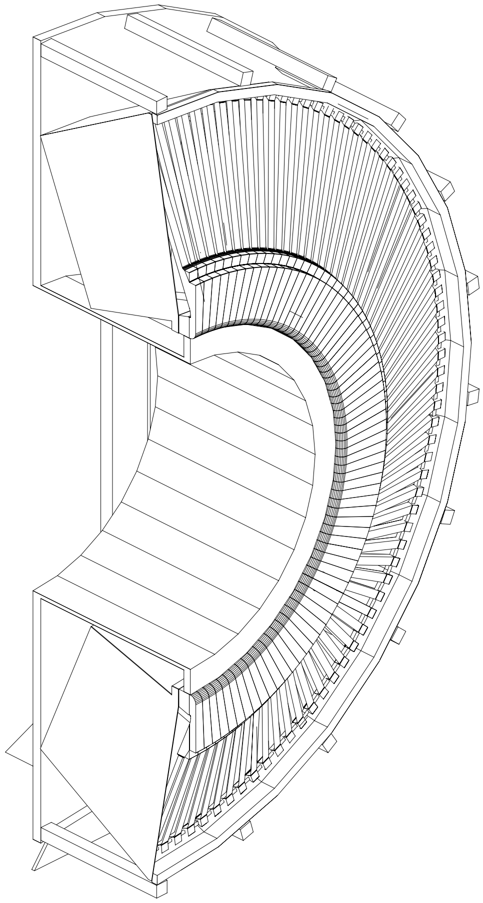

Figure 7-33. *Section of endcap container showing assembly jig and rails.*

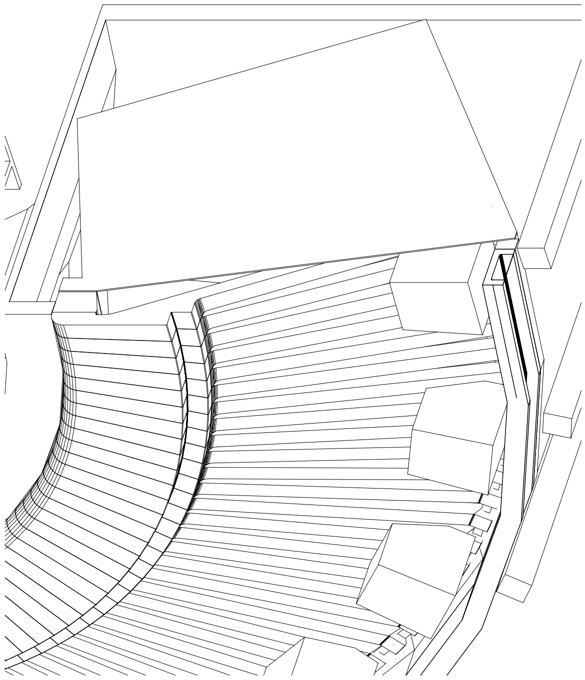

Figure 7-34. *Detail of endcap support structure showing ADC housings.*

finite-element analysis, and differences fed back into the model to enable modification of the final endcap design.

Endcap Installation into the Coil. The endcap halves are carried to the assembly area in the detector hall. A system test is done to verify that the endcap has not been damaged in transport. Installation of the endcap halves is discussed in Chapter 14. Figure 7-35 shows the barrel and half of the endcap installed in the detector.

7.7 Optimization and Prototype Studies

Optimization and prototype studies consist of testing and refining individual calorimeter components as they are designed and built, as well as system tests. The system tests will consist of two beam tests. The first will primarily examine the optical elements and front-end electronics, while the second will feature a full system prototype. It is anticipated that the first beam test will occur in the fall of 1995, and that the second will occur prior to full production, in the spring of 1996. Potential beam test sites in the US and Europe are

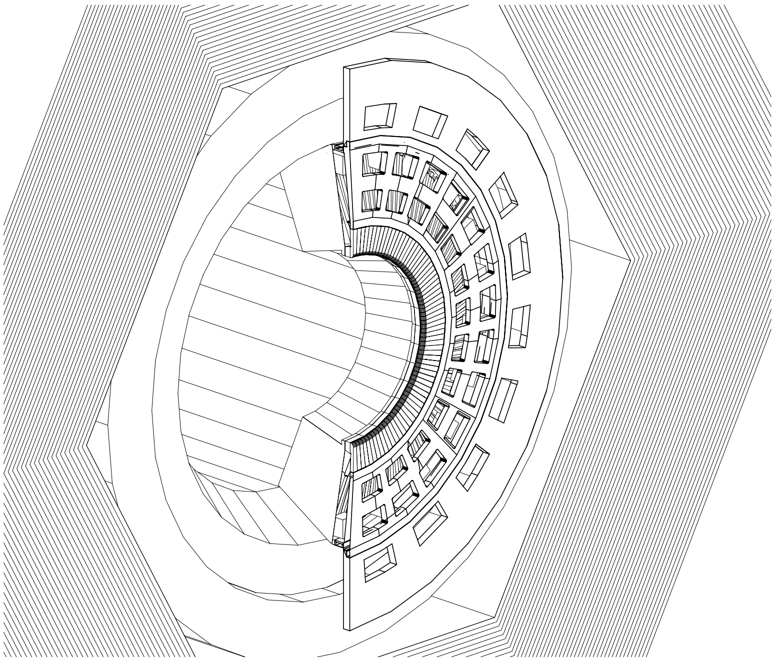

Figure 7-35. *Side view of mated barrel and half of endcap.*

being evaluated. Test-site selection criteria include the availability of low-energy beams to measure the effect of electronic noise on resolution and the availability of mixed beams of electrons and pions to test e/π separation and the effect of hadronic split-offs.

In the first beam test, it is anticipated that we will use an array of 5×5 crystals that have been tuned and wrapped in the manner planned for the actual calorimeter crystals. The optical elements to be tested consist of a photodiode and wavelength shifter readout, and the front-end electronics consists of the preamplifier/shaper amplifier package. To study their performance, these components will be tested in a realistic environment. The boxes used to hold each crystal will be made of the same materials as are planned for the actual mechanical support structure. The front-end electronics and its shielding will be those planned for the calorimeter. While not the final production version, an electronics cooling system will be implemented to obviate the effects of heating on the photodiode and electronics noise performance. Peak-sensing ADCs with a 12–13 bit resolution will most likely be used, rather than a prototype ADC. We will also not attempt to prototype the trigger and data acquisition system for this beam test. Aside from studying the front-end electronics, this test is an opportunity to gain experience with handling crystals and with the effects of the mechanical support and shielding materials. We anticipate results showing the effects of electronics noise and interstitial material on position and energy resolution.

The second test will consist of a nearly full system prototype, prior to production. One or two prototype mechanical modules will be utilized. This will give us further experience with mechanical fabrication techniques and with the installation of crystals and front-end electronics into the modules. However, tests to verify the mechanical strength and viability of the support structure will be conducted separately as part of the development of the structure. Based on the results of the first beam test, an improved, final production version of the front-end electronics and shielding will be implemented, as will a final version of the cooling system and cable layout. It is anticipated that prototype ADCs featuring a 17–18 bit dynamic range, though not necessarily a production version, will be utilized along with DAQ boards. The second beam test will give us a realistic check of the entire readout chain and shielding and of the functionality of the support structure before production begins.

7.8 Crystal Procurement Issues

7.8.1 Radiation Hardness

The primary source of radiation for the CsI calorimeter is showers caused by beam-gas interactions or off-axis particles striking machine elements at or near the IR, not synchrotron radiation. The typical energies of the shower particles are in the MeV range. The expected dose level for the barrel calorimeter is $\sim$1 krad/yr, and for the forward endcap $\sim$10 krad/yr.

At $\sim$1 MeV, the photon attenuation length in CsI is $\sim$5 cm, or $2.7X_0$. The radiation dose is concentrated in the front 10–15 cm of the crystal. However, scintillation light produced deep in the crystal is also affected by radiation damage, as radiation damage results in the formation of color centers or absorption bands [Hol88], and our readout system collects light reflecting from the front and side crystal surfaces. Measurements of a small CsI(Tl) crystal under radiation indicate that CsI(Tl) is relatively radiation resistant (Fig. 7-36). However, larger samples from various vendors suffer a degradation in light yield [Hit92] when irradiated, perhaps due to impurities in large CsI(Tl) samples.

Since impurities in the CsI(Tl) salt may increase the likelihood for radiation damage in CsI(Tl) crystals, we will attempt to establish a technique for growing radiation-hard CsI(Tl) crystals by carefully controlling the purity of the salt. We will establish a radiation-hardness specification for crystal procurement as a final check of the finished crystals. We will investigate the role of impurities in CsI(Tl) salt by measuring crystal samples doped with known impurities. We will study the role of crystal processing in the development of radiation-hard crystals. To determine trace elements and defects in the crystal, material characterization studies and micro-structural analyses will be performed. We will also study the light yield, scintillation, transmittance, and absorption of these CsI(Tl) crystals. If

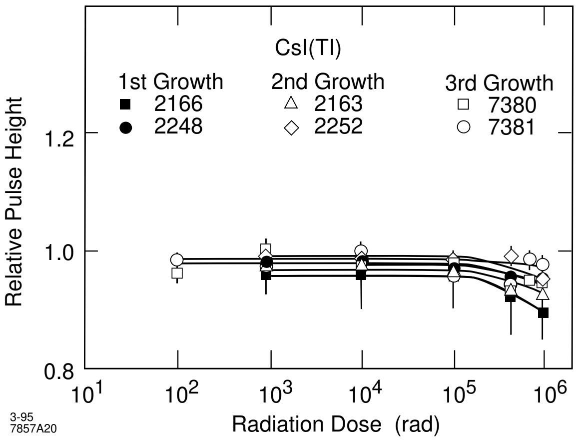

Figure 7-36. *Relative light yield of small (2.54×2.54 cm^2) Q&S CsI(Tl) crystals vs. radiation dose, measured with an avalanche photodiode with 1.275 MeV γs from a ^{22}Na source.*

correlations can be established between radiation hardness and an absence of impurities in the salt and/or the crystal growing process, this understanding can be incorporated into the growth of the crystals produced for the BaBar calorimeter.

Radiation hardness specifications for crystal procurement will be established to check the crystals supplied by vendors. A high dose test will be performed on small (2.54 cm cylinders) samples from production boules. A sample will receive a short-term dose of 20 krad, after which its light output will be measured. We require that the light output diminish by less than 20%, and that it recover within five days to within 5% of the light output measured prior to irradiation. Large crystals may be tested for uniformity of transmission as well as light output as a function of time.

In addition to the high-dose radiation measurements, we will carry out long-term (~12 months), low-dose (~1-3 rad/d) radiation studies using a modest number of production crystals from each supplier, selected after a consistent production quality has been established. These crystals will be placed in an environment similar to the one planned for the calorimeter (enclosure with dry-nitrogen flow, such that the relative humidity is $\leq$ 3% at room temperature) and irradiated from the front with a ^{137}Cs source. The gain and resolution of these crystals and a set of control crystals kept in the same type of environment but without radiation exposure will be monitored throughout the irradiation period. This test will help us distinguish radiation damage effects from aging effects.

7.8.2 Quality Control and Testing

Obtaining the desired energy resolution from the calorimeter will require strict control over the quality of the 6780 crystals, which will be of different types and from different manufacturers.

As the crystals are produced by the manufacturer, the following tests will be applied, and unsatisfactory crystals will be rejected.

- The dimensions of the crystal will be measured to ensure that they lie within the required mechanical tolerances;
- Each crystal will be visually inspected for flaws;
- The light output from a standard source at several positions along the polished and wrapped crystal will be measured using a standard readout system; this will measure the overall light yield and the variation with position; and
- Samples of the melt will be analyzed for trace impurities.

These tests will be carried out at the point of manufacture by the manufacturer working in close liaison with representatives from the collaboration calorimeter group. The exact details of the tests (which are still under study) will be specified as part of the purchase contract.

Immediately prior to assembly at the experiment, the crystals will be tested again, to confirm that the properties have not changed due to damage in transit or other causes.

Each accepted crystal will be assigned a unique identification number and its properties stored in a database. This will enable us to keep track of any batch-to-batch variations in the properties of crystals that may emerge during the course of the experiment.

References

[Ake92] E. Aker *et al., Nucl. Instr. Methods* **A321**, 69 (1992).

[Ale94a] R. Aleksan *et al.,* "Report of the *Ad Hoc* Calorimeter Committee," *BaBar Note* # 157 (1994).

[Ale94b] R. Aleksan *et al.,* "Resolution Studies Using GEANT," *BaBar Note* # 152 (1994).

[BaB94] "Letter of Intent for the Study of *CP* Violation and Heavy Flavor Physics at PEP-II," SLAC–443 (1994).

[BEL94] BELLE Collaboration, "Letter of Intent for a Study of *CP* Violation in *B* Meson Decays" (1994).

[Blu86] E. Blucher *et al., Nucl. Instr. Methods* **A249**, 201 (1986).

[Eis93] A.M. Eisner, "The Effect of Material *en route* to the EM Calorimeter," *BaBar Note* # 110 (1993).

[Fis87] F. Fischer *et al., Nucl. Instr. Methods* **A257**, 512 (1987).

[Gro84] D. Groom, "Silicon Photodiode Detection of Bismuth Germanate Scintillation Light," *Nucl. Instr. Methods* **A219**, 141 (1984).

[Hal95] G. Haller, D. Freytag, and J. Hoeflich, "Proposal for an Electronics System for the *BaBar* Calorimeter," *BaBar* Note #184 (1994).

[Hea94] C. Hearty, "Performance Comparison between CsI and LKr Calorimeters for PEP-II," *BaBar Note* # 141, (1994).

[HEL92] "HELENA, A Beauty Factory in Hamburg," DESY Report DESY 92/041 (1992).

[Hit92] D. Hitlin and G. Eigen, in Proceedings of the Int. Workshop on Heavy Scintillators for Scientific and Industrial Applications, edited by F. Nataristefani *et al.* (Editions Frontieres, 1992), p. 467.

[Hol88] I. Holl *et al., IEEE Trans. Nucl. Sci.* **35**, 105 (1988).

[Jes94] C. Jessop *et al.,* "Report on the Performance of Hex *vs.* Trapezoidal Crystals," *BaBar Note* # 215 (1994).

[Jes95a] C. Jessop *et al.,* "Development of the Front-End Readout for the *BaBar* CsI Calorimeter," *BaBar Note* # 216 (1995).

[Jes95b] C. Jessop *et al.,* "Reliability Issues for *BaBar* CsI Calorimeter," *BaBar Note* # 217 (1995).

[Kam83] T. Kamon *et al., Nucl. Instr. Methods* **A213**, 261 (1983).

[Kei70] G. Keil *et al., Nucl. Instr. Methods* **87**, 111 (1970).

[Kub92] Y. Kubota *et al., Nucl. Instr. Methods* **A320**, 66 (1992).

[Lev94] M. Levi, "Impact of Backgrounds on the Calorimeter Resolution," *BaBar Note* # 151 (1994).

[Lor86] E. Lorenz *et al., Nucl. Instr. Methods* **A239**, 235 (1986).

[Mil90] U.S. Military Handbook, "Reliability Prediction of Electronic Equipment" (1990).

[Sch94] R. Schindler, "Experimental Highlights of B meson Production and Decay," in L. Montanet *et al.,* Physical Review **D50**, 1601 (1994).

[Spi94] A. Spitkovsky and F.C. Porter, "Study of Light Transport in Different CsI Crystal Geometries," *BaBar Note* # 146 (1994).

[Zhu95] R. Zhu, "e/π Separation in the *BaBar* CsI Calorimeter," *BaBar Note* # 151 (1995).

[Zis91] "An Asymmetric B Factory Based on PEP," ed. by M. Zisman, SLAC–372 (1991).